A method for laser rangefinder reticle position calibration in a multi-sensor imaging system

Saša Vujić, *Member, IEEE,* Miloš Radisavljević, *Member, IEEE,* Dragana Perić, *Senior Member, IEEE* and Branko Livada, *Senior Member, IEEE*

***Abstract*— A method for laser rangefinder reticle position calibration in a multi-sensor imaging system is presented. This method was developed to provide system control software with proper parameters used for LRF reticle position, for all imagers and for different field of view configurations of those imagers in a typical multi-sensor imaging system. The importance of reticle position calibration and accuracy is explained, and error calculated. A prerequisite for laser rangefinder reticle position calibration is to perform each imager calibration and the multi-sensor imaging system optical axes rectification. The method is straight forward, fast and reliable. Details of the method are described and experimental verification of results obtained after the calibration are given.**

***Index Terms*—laser rangefinder; LRF; reticle calibration; multi-sensor imaging system; electro-optical system; long-range surveillance.**

I. Introduction

Multi-sensor imaging systems (MSIS) with zoom lenses are used for surveillance with number of technical, technological and application challenges [1], and also for other applications where observed object of interest (target) distance is important, e.g. target geolocation. These MSIS' functionalities are related with the use of laser rangefinders (LRF) and their proper integration within the MSIS [2], [3]. A control station – operator's console, which provides a user interface to MSIS sensors data, is another important part of MSIS [4]. In order to create a usable system it is necessary to provide a system operator with possibility to accurately point with LRF beam to desired object of interest. For this purpose it is necessary to determine control software parameters used for LRF reticle positioning. With properly determined parameters control software displays the LRF reticle at the right place and operator is able to direct the MSIS, i.e. the LRF beam to target, for any selected field of view (FOV).

Saša Vujić is with the Vlatacom Institute of High Technologies, 5 MilutinaMilankovića Blvd., 11070 Belgrade, Serbia (e-mail: sasa.vujic@vlatacom.com), and with the Belgrade Metropolitan University, Tadeuša Košćuška 63, 11000 Beograd, Serbia

Miloš Radisavljević is with the Vlatacom Institute of High Technologies, 5 Milutina Milankovića Blvd., 11070 Belgrade, Serbia (e-mail: milos.radisavljevic@vlatacom.com), and with the Belgrade Metropolitan University, Tadeuša Košćuška 63, 11000 Beograd, Serbia

DraganaPerić is with the Vlatacom Institute of High Technologies, 5 Milutina Milankovića Blvd., 11070 Belgrade, Serbia (e-mail: dragana.peric@vlatacom.com).

Branko Livada is with the Vlatacom Institute of High Technologies, 5 Milutina Milankovića Blvd., 11070 Belgrade, Serbia (e-mail: branko.livada@vlatacom.com).

This work is continuation of work published in [2] and [3], where LRF integration, LRF reticle integration and camera calibration are described. In available literature there are also other articles related to these topics [5-12], however, the details and methods about how to determine control software parameters used for LRF reticle positioning are not readily available, and therefore we are not able to make any comparison with other calibration methods in the sense of complexity and accuracy.

In this work the main research issue was to establish the correlation between LRF beam, images from different imagers and for any FOV, and reticle which is shown on display. Furthermore, the particular goal was to define a method for determining control software parameters used for LRF reticle position.

In this paper in section II we describe a typical electro-optical MSIS architecture and basic functionalities, in section III some zoom lens properties, in section IV we explain the importance of LRF reticle position calibration and its accuracy, in section V we list prerequisites for LRF reticle calibration, in section VI we present a method for LRF reticle position calibration in a multi-sensor imaging system, in section VII we summarize results of the method experimental verification, and in section VIII we give the conclusion.

II. Electro-optical multi-sensor system architecture and basic functionalities

Multi-sensor imaging systems (MSIS) are used for surveillance, observed object geolocation and other applications [13], [14]. Each of those systems comprises an electro-optical head with integrated sensors mounted on a gimbal, and remote operator's console with application software for monitoring and control [4].

A typical MSIS with MWIR thermal imager, visible light imager and a LRF mounted on a gimbal is shown in Fig. 1.

Fig. 1. Multi-sensor imaging systems with laser rangefinder.

The sensors that those systems usually comprise [1] are

 ISBN 978-86-7466-930-3

midwave infrared (MWIR) or longwave infrared (LWIR) thermal imagers with continuous zoom optics, visible light imagers with continuous zoom optics, short-wave infrared (SWIR) imagers with continuous zoom optics, laser rangefinders (LRF), positioning sensors and orientation sensors. Such systems are capable of measuring the line of sight distance from the electro-optical head with sensors to some object of interest, by using a LRF, and are also capable to accomplish many other more advanced tasks, e.g. calculating observed object of interest geolocation, based on known data about MSIS position, orientation and observed object distance [15-17].

A MSIS operator uses such a system through an operator's console with input and output devices, via a graphical user interface (GUI) which is a part of a software application for monitoring and control installed on the operator's console [4]. The operator's console can be in different forms, with one or more displays as output device, and with joystick, touchpad, trackball, touchscreen, keyboard or mouse as input device. An example of operator's console is shown in Fig. 2.

Fig. 2. Multi-sensor imaging system operator's console with three displays.

The GUI provides video streams for each of the integrated imagers, as well as other data, statuses and controls for MSIS functionalities. Depending on the selected operator's console for the particular application, the GUI is usually optimized to provide the best possible usability in a given scenario. An example of GUI with two video streams, map, statuses and controls is shown in Fig. 3.

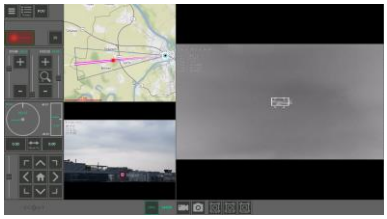

Fig. 3. Graphical user interface (GUI) of an operator's console, with two video streams, map, statuses and controls.

For each of the video streams there is an option to display a LRF reticle which shows the operator where the LRF beam is aiming. A video stream with reticle is shown in Fig. 4.

In order to bring such a system into the function there is a need to perform calibrations on different levels, including the continuous zoom imagers' calibration. One of the calibration tasks is to perform a calibration of LRF reticle position coordinates, for each imager, for different zoom levels. Before performing this reticle position calibration it is necessary to perform optical axes alignment to set up the axes of all imagers and LRF to be parallel to each other (a process called optical axes rectification, or boresighting).

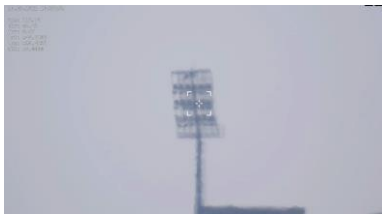

Fig. 4. Video stream with LRF reticle (object distance 4320m).

The optical axes rectification process is performed by means of precise mechanical positioning of structures holding optical elements. The optical axis rectification process is performed with zoom optics set in high end position, which gives a narrow field of view (NFOV), in order to achieve better accuracy. However, other fields of view (FOV) are also of interest and in order to provide a proper alignment of reticle for different zoom levels (different FOVs) there is a need to calibrate reticle position for different zoom levels due to an inherent characteristic of zoom lens to have deviation of optical axis from the ideal one when changing the zoom level. Therefore, the process of optical axis rectification does not have to be perfect and several pixels displacement can be allowed. Those displacements can be compensated by means of precision positioning of reticle in the image, i.e. in each frame of the video streams. The size of the reticle corresponds to the solid angle of the LRF beam. A typical LRF reticle, as drawn on visible light imager is show in Fig. 5.

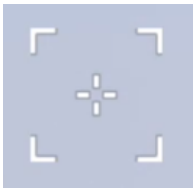

Fig. 5. LRF reticle as shown on screen

The process of reticle position coordinates calculation for all imagers and for different FOVs is time consuming and requires highly skilled operators and their high concentration, with high risk of making mistakes during the process. Therefore, in Vlatacom Institute we developed a method for LRF reticle position calibration such that the whole process is straight forward, fast and not prone to random errors.

III. ZOOM LENS PROPERTIES

Zoom lenses are very popular in modern multi-sensor imaging systems used in long-range surveillance and related applications. They provide flexibility and controllability for different missions and use cases. Zoom lenses provide users with a functionality to observe areas with any FOV angle, from a wide field of view (WFOV) to NFOV, and also to focus objects on different distances from minimal object distance (MOD), to infinite distance, for any FOV. Some of

 ISBN 978-86-7466-930-3

the basic properties of each zoom lens are minimal and maximal focal length - f_{min} and f_{max}, f-number - N, WFOV, NFOV and MOD. There are also many others which define lens optical characteristics and electro-mechanical interfacing.

WFOV and NFOV of imager depend on imaging sensor size and minimal/maximal lens focal lengths. WFOV, NFOV of two MSIS, C330 and C1000, are given in Table I.

TABLE I
CONTINUOUS ZOOM LENS PARAMETERS OF TWO THERMAL AND TWO VISIBLE LIGHT IMAGERS

Lens\Par.	WFOV [°]	NFOV [°]	f_{min} [mm]	f_{max} [mm]
C330-VIS	36	3.5	16	160
C330-TH	35.4	1.67	16	330
C1000-VIS	21	0.55	20	800
C1000-TH	18	0.75	40	1000

The thermal imager resolution is 640 x 480 with pixel size of 15 μm for C330-TH, and 1280 x 1024 with pixel size of 10 μm for C1000-TH.

One of the important properties is back focal length (BFL), also known as flange focal distance (FFD), flange focal depth (FFD), flange back distance (FBD), flange focal length (FFL). BFL defines the position of the zoom lens focal plane distance, where the imaging sensor plane should be placed, and the lens mounting reference plane. The adequate distance of the imaging sensor will result in the a possibility to focus objects from MOD to infinite distance, for any FOV from WFOV to NFOV. A typical test target used for back focus calibration, USAF 1951, is show in Fig. 6.

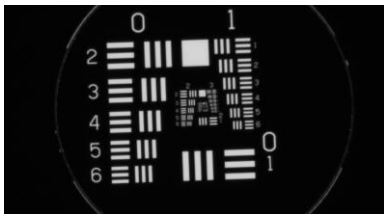

Fig. 6. USAF 1951 test target used for back focus calibration.

The zoom lens functionality is based on moving mechanisms which inherently involve lens elements displacements relatively to their ideal positions. For this reason it is necessary to perform additional zoom lens calibration for proper alignment of LRF reticle with LRF beam [17-21].

All these calibrations are necessary for successful LRF integration in any MSIS [2], [3].

Instantaneous field of view or (IFOV) is an important parameter which determines how much a single pixel can see in terms of FOV, depends on pixel size and focal length and equals IFOV = Pixel Size / Focal Length. With zoom lenses IFOV changes with FOV from wide IFOV(f_{min}) to narrow IFOV(f_{max}) angle.

IV. THE IMPORTANCE OF RETICLE CALIBRATION AND ITS ACCURACY

The LRF beam is quite narrow with Gaussian distribution [2] and in tested systems it is circular in shape with divergence angle of 700 μrad in case of MSIS C330, and 250 μrad in case of MSIS C1000. Both are eye safe with 1,54 μm wavelength. The maximal measurement ranges are 20 km and 39 km, with range measurement accuracy of ±5 m, and ±1 m respectively. The minimal IFOV (at NFOV) in tested systems is 32 μrad in case of MSIS C330, and 5 μrad in case of MSIS C1000. For these cases the LRF beam divergence is 22 to 50 pixels.

If the LRF reticle was not well aligned with the LRF beam the LRF functionality would be lost, due to the fact that LRF beam would miss the target, i.e. it would not hit the area where the MSIS operator is targeting with the reticle, resulting in a wrong measured data, or no measurement at all. If the reticle was quite well aligned with the beam, but not perfectly, it would be possible to measure the object distance, but for any mistake or deviation in misalignment between the reticle and LRF beam an added error in geolocation calculation [16] would be made. With MSIS C330, at 10 km distance, the error introduced with reticle misalignment is 0,32 m for each pixel of reticle displacement. Therefore, the accuracy of reticle positioning is important for such systems. In a simplified model of MSIS, the LRF beam is an ideal line corresponding to the center of the reticle shown on the screen. However, in real case the center of LRF beam will not match ideally to the reticle center, as shown in Fig. 7.

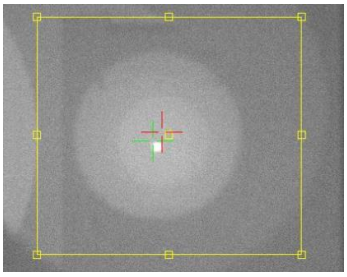

Fig. 7 Displacement of reticle and LRF

For some real MSIS and long distances at which these systems are used, the error that is made due to the reticle displacement can be significant. The error in geolocation calculation for one pixel of reticle displacement on real systems for four different imagers given in Table I, at distances of 1, 2, 5, 8 and 10 km, are given in Table II.

TABLE II
ERROR IN GEOLOCATION CALCULATION FOR ONE PIXEL OF RETICLE DISPLACEMENT AT DISTANCES OF 1, 2, 5, 8 AND 10 KM, IN MM

Error in mm	Distance				
Imager	1km	2km	5km	8km	10km
C330-VIS	32	64	159	255	318
C330-TH	46	91	228	364	455
C1000-VIS	5	10	25	40	50
C1000-TH	10	20	51	82	102

 ISBN 978-86-7466-930-3

The error in geolocation calculation at object distance of 10 km, for 1, 2, 5, 8 and 10 pixels of reticle displacement on real systems for four different imagers given in Table I, are given in Table III.

TABLE III
ERROR IN GEOLOCATION CALCULATION AT 10KM DISTANCE FOR RETICLE DISPLACEMENTS OF 1, 2, 5, 8 AND 10 PIXELS, IN M

Error in m	Displacement				
Imager	1 px	2 px	5 px	8 px	10 px
C330-VIS	0,32	0,64	1,59	2,54	3,18
C330-TH	0,46	0,91	2,28	3,64	4,55
C1000-VIS	0,05	0,10	0,25	0,40	0,50
C1000-TH	0,10	0,20	0,51	0,82	1,02

V. THE PREREQUISITES FOR LRF RETICLE CALIBRATION

A prerequisite for LRF reticle calibration is to perform each imager "zoom to FOV" calibration [2]. Depending on non-linearity of imager lens characteristic it is necessary to decide the number and value of discrete zoom lens positions for which the reticle will be calibrated. For all other zoom lens positions, in between the selected discrete positions, the reticle position will be calculated during the run time in the software application, using piecewise-linear approximation.

Furthermore, it is necessary to perform MSIS optical axes rectification, by means of precise mechanical positioning of structures holding optical elements, which is usually performed in NFOV setup for each imager. This way we will ensure that the calibrated MSIS will have the full correspondence of each imager reticle presenting the area where the LRF beam is aiming. In the ideal case the beam central line will correspond to each reticle central point. When the optical axes are nearly parallel, which can be observed and confirmed with use of collimator (few pixels displacement can be tolerated), a procedure of LRF reticle position calibration can be started.

It is necessary to perform the described procedure for each of the imagers contained in the MSIS. The sequence of the imagers' reticle calibration is irrelevant. Therefore the procedure can be started with any of the imagers that are contained in the MSIS. A MSIS set up in front of the collimator for rectification of visible light imager with LRF is presented in Fig. 8.

Fig. 8 A MSIS set up for rectification of visible light imager in front of the collimator

If the LRF is equipped with properly aligned visible light boresighting LED source, it can be used to make LRF reticle calibration, instead of LRF emitter. In that case instead of capturing videos a single image can be captured for each FOV. The same method can be used for LRF devices that can operate in continuous measurement mode (CMM). A single image will be sufficient for determining of LRF beam central point.

VI. A METHOD FOR LRF RETICLE POSITION CALIBRATION IN A MULTI-SENSOR IMAGING SYSTEM

Within this method there are four stages to be completed. In the first stage the raw data should be captured, then in the second stage the position of LRF beam in the target should be determined, for each FOV. In the third stage the reticle calibration parameters should be calculated, and finally in the fourth stage the calibration parameters should be entered into software application that draws the reticle in the video stream.

For the first stage we need a device under test (DUT), in this case a selected imager, and an appropriate collimator for the selected imager's maximal focal length. In Fig. 9 an image taken with visible light imager of LRF firing in a target is shown.

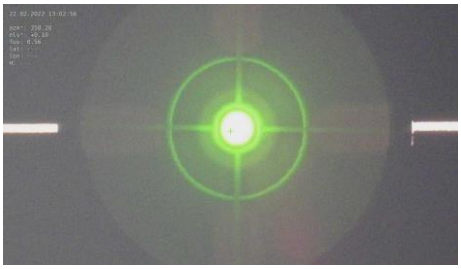

Fig. 9. Image taken with visible light imager of LRF firing in a target

All steps of the first stage are shown in block diagram in Fig. 10.

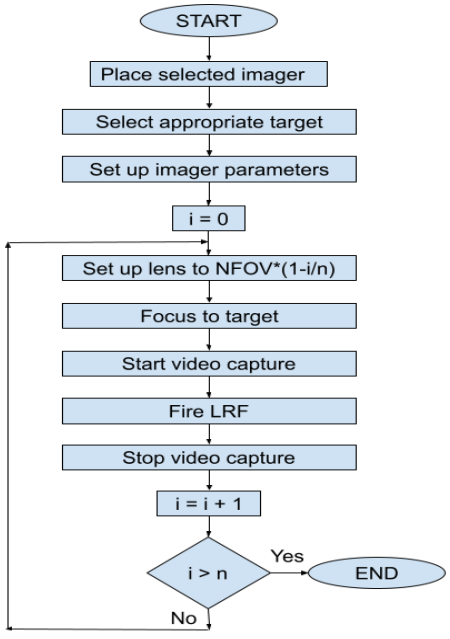

Fig. 10. Block diagram for first stage of the LRF calibration

 ISBN 978-86-7466-930-3

The procedure is then repeated for each of the imagers contained in the MSIS.

When all videos are captured, for all imagers, then the first stage of this process is finished and the second stage can start. In the second stage for each captured video from the first stage we extract a frame in which the LRF beam is clearly visible. From that frame we determine the central coordinates of the LRF beam relatively to the image center.

In Fig. 11 an image taken with visible light imager of LRF firing in a target is shown.

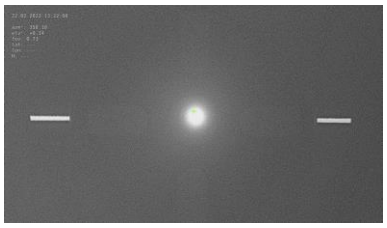

Fig. 11. Image taken with thermal imager of LRF firing in a target

For small angles close to NFOV the displacement from the image central coordinates to the LRF beam central coordinates depend on precision of optical axes rectification performed in previous stage. For wider angles closer to WFOV the displacement of LRF beam central coordinates depend on lens' construction. That can be seen also on the Fig. 12 where the reticle displacement in pixels for visible light and thermal imager are shown, for x and y axes. In case of visible imager the displacements are in range from 0 to 29 pixels in x axis, and from -6 to 29 pixels in y axis. In case of thermal imager the displacements are in range from -7 to 4 pixels in x axis, and from -1 to -12 pixels in y axis. In this case the displacements are higher for visible light imager due to the fact that its IFOV is twice smaller then in thermal imager.

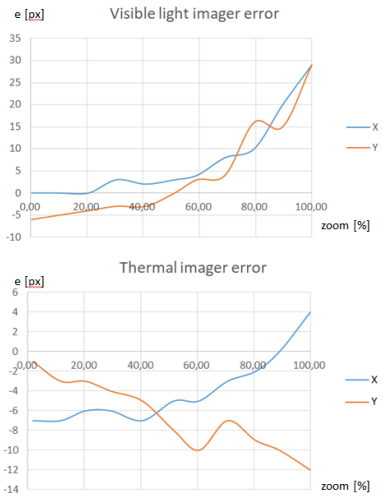

Fig. 12. Reticle displacement in pixels for visible light and thermal imager

When we have central coordinates for all imagers for each selected FOV, then in stage three we calculate reticle positioning parameters. As a result we have x and y reticle positioning parameters for each imager.

Finally, in stage four, the reticle positioning parameters can be entered into the software application that draws the reticle in the video stream.

By default, without the calibration, the reticle is drawn in the center of the video stream for any FOV. Only after the calibration parameters are entered the reticle will be drawn displaced to the image center, corresponding to the relative displacement of the LRF beam for any selected FOV.

VII. Results of Experimental Verification

The proposed method for LRF reticle position calibration has been verified in real conditions using available MSIS. The MSIS has been placed on the rooftop of the building from where there is a good view on existing remote objects.

Fig. 13. A heating plant chimney at 8km distance used to verify the x-axis deviations of the reticle, in thermal and visible imager

The most appropriate objects for verification of LRF beam correspondence with reticle position on the screen are those objects which have large and sharp edges. It is important to use remote objects on relatively long distances, in order to minimize error due to non-coaxial quasi parallel axes of

 ISBN 978-86-7466-930-3

imagers and LRF.

In this particular case a heating plant chimney at 8km distance was used to verify the x-axis deviations of the reticle from the ideal case in NFOV. Images taken with thermal and visible light imagers are shown in Fig. 13.

For verification of y-axis a rooftop heliport structure with upper and lower limits, at the distance of 620m was used as shown in Fig. 14.

Fig. 14. A rooftop heliport structure with upper and lower limits, at the 620m distance, used to verify the y-axis

Several LRF measurements have been accomplished in order to confirm where the LRF beam is really aiming and to verify the good correspondence with the LRF reticle on the screen. It has been shown that deviation is equal to 2 pixels in thermal imager, which in this case corresponds to 0.1 mrad, and 3 pixels in color imager, which in this case corresponds to 0.15 mrad.

Furthermore, it has been shown that for other FOVs reticle deviation from the ideal one is similar in pixel size, but is lower in angle, due to larger FOV angles.

VIII. Conclusion

The described method was implemented to provide straight forward, fast and reliable process of reticle position calibration. The calibration process is complex but with this method it is straight forward, and can be performed by trained personnel. It is fast allowing efficient use of expensive equipment. Furthermore, it is reliable resulting in high process efficiency. However, there is a need for further work on additional improvements in process of reticle calibration. The further work will focus on automatic extraction of LRF spot central coordinates based on image processing techniques which can be applied on the same images taken during the reticle calibration process.

Acknowledgment

Authors would like to thank Vlatacom Institute for equipment and support which enabled continuous work and improvements in the field of electro-optics. This work was undertaken within the Vlatacom Institute project P157.

References

[1] D. Perić, B. Livada, „Technical, technological and application limitations of the electro-optical surveillance systems“, 8th International Conference on Defensive Technologies, OTEH 2018, Belgrade, Serbia, 11-12 October 2018

[2] B. Livada, D. Perić, M. Perić, „Challenges of Laser Range Finder Integration In Electro-Optical Surveillance System“, 4th International Conference on Electrical, Electronic and Computing Engineering IcETRAN 2017, Kladovo, Serbia, June 05 – 08, 2017

[3] B. Tomić, D. Perić, M. Radisavljević, S. Vujić, „Reticle Integration and Camera Calibration in Multi Sensor Surveillance Systems“, 8th International Conference on Defensive Technologies, OTEH 2018, Belgrade, Serbia, 11-12 October 2018

[4] D. Perić, S. Vujić, B. Livada, „Multi-sensor system operator's console: Towards structural and functional optimization“, 7th International Conference on Defensive Technologies, OTEH 2016, Belgrade, Serbia, 6-7 October 2016

[5] S. M. Ayaz, M. Y. Kim, J. Park, Survey on zoom-lens calibration methods and techniques", Machine Vision and Applications, July 2017

[6] A. Pennisi, D. Bloisi, C. Gaz, L. Iocchi, D. Nardi, "Novel Patterns and Methods for Zooming Camera Calibration", Journal of WSCG, Volume 21, Number 1, 2013, pp. 59-67

[7] Z. Wu, and R. J. Radke, "Keeping a Pan-Tilt-Zoom Camera Calibrated", IEEE Transactions on Pattern Analysis and Machine Intelligence, November 2012

[8] S. Upadhyay, S.K.Singh, M. Gupta, A. K. Nagawat, "Linear and Non-linear Camera Calibration Techniques", Journal of Global Research in Computer Science, Volume 2, No. 5, April 2011

[9] B. Wu, H. Hu, Q. Zhu, and Y. Zhang, "A Flexible Method for Zoom Lens Calibration and Modeling Using a Planar Checkerboard", Photogrammetric Engineering & Remote Sensing, Vol. 79, No. 6, June 2013, pp. 555–571

[10] Z. Wang, J. Mills, W. Xiao, R. Huang, S. Zheng and Z. Li, "A Flexible, Generic Photogrammetric Approach to Zoom Lens Calibration", Remote Sens. 2017, 9, 244

[11] S. Zheng, Z. Wang, R. Huang, "Zoom lens calibration with zoom- and focus-related intrinsic parameters applied to bundle adjustment", ISPRS Journal of Photogrammetry and Remote Sensing 102 (2015), pp. 62–72

[12] Reg G. Willson, S. A. Shafer, "What is the center of the image?", J. Opt. Soc. Am. A ,/ Vol. 11, No. 11/, November 1994

[13] J. Y. Dufour (Editor), Intelligent Video Surveillance Systems. ISTE Ltd. London and John Wiley & Sons Inc., New York, 2013

[14] A. K. Maini, Lasers and Optoelectronics: Fundamentals, devices and applications, John Wiley and Sons, Chicheste,. UK, 2013

[15] J. A. Ross, B. R. Geiger, G. L. Sinsley, J. F. Horn, L. N. Long, and A. F. Niessner: " Vision-Based Target Geolocation and Optimal Surveillance on an Unmanned Aerial Vehicle", AIAA Paper 2008-7448, AIAA Guidance Navigation and Control Conference, Honolulu, Hawaii, 2008

[16] Livada, B.; Vujić, S.; Radić, D.; Unkašević, T.; Banjac, Z. Digital Magnetic Compass Integration with Stationary, Land-Based Electro-Optical Multi-Sensor Surveillance System. Sensors 2019, 19, 4331. https://doi.org/10.3390/s19194331

[17] B. Livada, S. Vujić, „Target position CEP50 estimation using electro-optical multisensory surveillance system", 8th International Conference on Defensive Technologies, OTEH 2018, Belgrade, Serbia, 11-12 October 2018

[18] D.C. Dilworth, "A zoom lens from scratch: the case for number crunching", Proc. SPIE 9947, Current Developments in Lens Design and Optical Engineering XVII, 994702 (27 September 2016)

[19] R. N. Youngworth and E. I. Betensky, "Fundamental Consideration for zoom lens Design (tutorial)", Proc. SPIE, Vol. 8488, Zoom Lenses IV, 2012

[20] Rowlands, D. Andrew, Field guide to photographic science, SPIE Press, Bellingham, USA, 2020

[21] S. Zhou and L. Jiang: "A modern description of Rayleigh's criterion", Phys. Rev. A , 99, 013808, 2019.

 ISBN 978-86-7466-930-3

Linear regression in RR-RT domain for cardiac cycle evaluation

Milan S. Milivojević, *Student Member, IEEE*, Ana Gavrovska, *Member, IEEE* and Dragi Dujković, *Member, IEEE*

***Abstract*—Analysis of cardiac variability is of great importance for numerous applications. Among them are the ones based on electrocardiograms where detection of distorted signals during the acquisition process can be performed as well as discrimination of pathological records due to various diseases. One way of presenting the cardiac variability relates to parameters derived from the time duration of the respective segments within the electrocardiogram cycle as well as their relationships. In this paper, cardiac cycle evaluation is performed in the domain of time features for the assessment of cardiac variability using the linear regression procedure. The calculated quotient shows the possibility to be useful in terms of error polarity.**

***Index Terms*—Electrocardiogram (ECG), cardiac cycle, R peak, T wave, quotient, linear regression.**

I. Introduction

The cardiac cycle is a series of pressure changes that take place within the heart. These pressure changes result in the movement of blood through different chambers of the heart and the body as a whole. They originate as conductive electrochemical changes within the myocardium that result in the concentric contraction of cardiac muscle [1]. The cardiac cycle can be divided into two phases: the systole phase and the diastole phase. During the systole phase heart muscle contracts and blood is pumped into the arteries. For electrocardiogram (ECG) this phase is manifested in the form of QRS complex appearance (associated with ventricular depolarization) and T waves (ventricular re-polarization). Diastole phase follows systole and represents relaxation of the heart muscle where the heart is filled with blood. Diastole can be identified on the electrocardiogram through the appearance of the P wave, which is further related to atrial depolarization [2].

Besides standard analysis of RR intervals (time intervals between successive R peaks), cardiac variability can be observed through intervals that describe the phase of diastole or systole. The characteristic points that divide the cardiac cycle into two phases are the R peak and the end of the T wave. There are different variants of interval definitions in the literature that are specific for these phases, which also include Q or S wave [3]. Since detection of the maximum within a cycle (R peak) is the basic procedure in ECG signal processing, R peak is taken as the point that defines the boundary between systole and diastole. Therefore, RT and corresponding difference between RR and RT intervals are considered to be suitable for the ventricular systole and ventricular diastole phases. Appropriate relationships derived from these intervals are the basis for the evaluation of cardiac cycles in electrocardiogram signal.

The golden ratio or cross-section represents a constant ϕ with an approximate value of 1,6180339887… This relationship has been known since ancient times as a principle in art from antiquity through the Renaissance to the present day. However, it is interesting that this relationship can be found in nature in organic and inorganic structures. Mathematical definition of the golden ratio ranges from the inherent geometric definition to the definition that includes extended fractions and series [4].

In this paper, a linear regression is performed in the domain of ECG time intervals (RR and RT intervals) in order to differentiate cases, like male and female individuals. Signals are taken from publically available Physionet data which includes healthy volunteers. A comparison of calculated direction coefficients obtained by the regression procedure with the reference representing the golden ratio constant is performed.

The work is organized into five sections. Section II presents the materials and methods applied in the paper. In Section III the experimental analysis is described. The results of the analysis are given in Section IV. Finally, Section V presents a conclusion with a note on further work.

II. Material and Methods

A. Golden Ratio Definition

Fibonacci array can be defined as a collection of elements where each array element value equals to the sum of the previous two elements of the array. Initial values of the first two members of the sequence are equal to 1. If limit value of the quotient of two consecutive members of the Fibonacci sequence is observed, a constant, here noted as ϕ, can be defined. This is illustrated in Fig. 1.

This constant describes the golden ratio [5]:

$$\lim_{n\to\infty}\frac{x[n+1]}{x[n]}=\phi=1.61803399... \tag{1}$$

Milan Milivojević is with the University of Belgrade School of Electrical Engineering, Bulevar kralja Aleksandra 73, 11120 Belgrade, Serbia (e-mail: milansmilivojevic@gmail.com), and the Academy of Technical and Art Applied Studies Belgrade, Department School of Information and Communication Technologies, Zdravka Čelara 16, 11000 Belgrade, Serbia (e-mail: milan.milivojevic@ict.edu.rs) (https://orcid.org/0000-0001-6814-9520).

Ana Gavrovska is with the University of Belgrade - School of Electrical Engineering, Bulevar kralja Aleksandra 73, 11120 Belgrade, Serbia (e-mails: anaga777@gmail.com; anaga777@etf.rs), (https://orcid.org/0000-0003-2740-2803).

Dragi Dujković is with the University of Belgrade - School of Electrical Engineering, Bulevar kralja Aleksandra 73, 11120 Belgrade, Serbia (e-mail: dragi@etf.rs).

 ISBN 978-86-7466-930-3

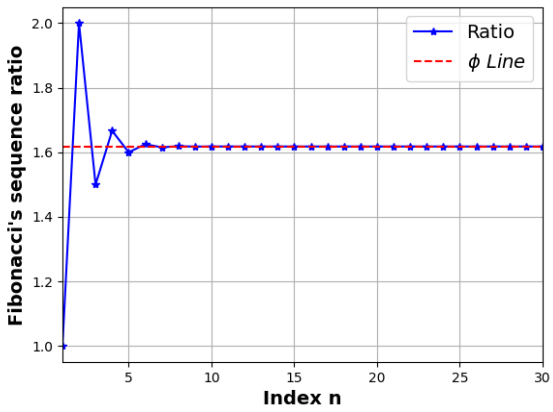

Fig. 1. Fibonacci sequences convergences.

The constant value ϕ can also be reached geometrically by dividing a segment into two parts. Let the lengths of the first and the second segment be noted as *a* and *b*, respectively. The segments are said to make a golden ratio if the ratio is as:

$$\frac{a+b}{a} = \frac{a}{b} = \phi . \tag{2}$$

The previous equation can be written in the form of the golden ratio characteristic equation:

$$\phi^2 - \phi - 1 = 0 \tag{3}$$

where solution leads to the exact value of the constant ϕ which is also equal to the positive solution of the quadratic equation:

$$\phi = \frac{1+\sqrt{5}}{2} . \tag{4}$$

B. Dataset

PhysioBank is a large and growing archive of digital recordings of physiological signals and corresponding data for biomedical and similar research. In this paper ECG-ID Database from Physionet is used for the analysis [6].

The database contains 310 ECG recordings, obtained from 90 individuals. Each record contains one electrocardiogram channel of twenty seconds duration and 12-bit resolution with 500Hz sampling frequency. The signal amplitude is within interval from -10mV to +10mV. The records were obtained from volunteers (44 men and 46 women aged from 13 to 75 years). The number of records per each person varies from two (collected during one day) to twenty (collected periodically over 6 months). The raw ECG signals are rather noisy and contain both high and low frequency noise components. Each record includes both raw and filtered signals. In the simulation presented in this paper only raw ECG signal are used [7].

C. Software Tools

For the purposes of this work, Python 3 programming language is used, as well as the corresponding libraries, among which the Neurokit2 library stands out. NeuroKit2 is an open-source, community-driven, and user-centered Python package for neurophysiological signal processing. It provides a comprehensive suite of processing routines for a variety of bodily signals like ECGs [8].

III. Experimental Analysis

Within electrocardiogram (ECG) signal, three basic parts can be distinguished: P wave, QRS complex and T wave. Sometimes U wave is also visible. These waves are result of non-homogeneities of action potentials throughout the heart. They are directly related to the start time of depolarization and the time course of the action potential. The waves Q, R and S are manifestation of the depolarization in the two ventricles, while the waves T and U are consequence of the repolarization process in the ventricles [9].

Depending on the application, appropriate features can be extracted from the signal itself. In this paper, the focus is on finding the appropriate relations of the golden section, where temporal features are found [10].

Here, electrocardiogram signals from different volunteers are analyzed. Each signal is preprocessed, and this is followed by the detection of characteristic points. Based on the detected points, the corresponding time intervals (timestamps) are found as valuable features expressed in seconds. Based on two time intervals that are selected for each cardiac cycle, quotient value is estimated using the appropriate definition as well as in the form of direction coefficient obtained using the linear regression procedure. The values of this quotient are compared with the value given by the golden ratio constant.

A. Preprocessing

As a first step, pre-processing of the original ECG signal was performed to remove unwanted signal components. These components primarily include muscle noise, 50 Hz network noise, and baseline deviation [11]. Noisy raw signals are chosen to observe practical importance of the ratio base relations between the waves. In order to suppress the interferences, a band-pass filter with a finite impulse response and a zero phase has been applied. The lower and upper bandwidth limits have been set to 0.3 Hz and 45 Hz, respectively. In Fig. 2 examples of raw signal from ECG-ID database and preprocessed signal are presented.

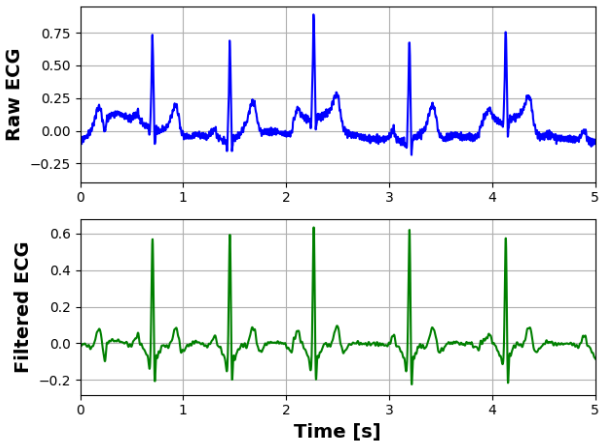

Fig. 2. Raw and preprocessed ECG signal.

B. ECG based interval determination by characteristic point detection

After the preprocessing step, characteristic points in time domain are found. Namely, for the experimental analysis

 ISBN 978-86-7466-930-3

two characteristic points are detected: R peaks and the moment corresponding to the end of the T wave (T wave offsets). The detection of these points is based on the wavelet method using functions from the Neurokit2 library [12]. The time intervals between two consecutive R maxima define the sequence of RR intervals.

For each RR interval, an additional time interval RT is found. It corresponds to the difference between the time moments of the end of the T wave and the corresponding R maximum. Since R peaks are relatively easy to detect T wave offsets can be considered also as fiducial points for further analysis. Figure 3 illustrates the detection of characteristic points in Fig.3 (a) as well as the determination of RR and RT time intervals based on detected characteristic points in Fig.3 (b).

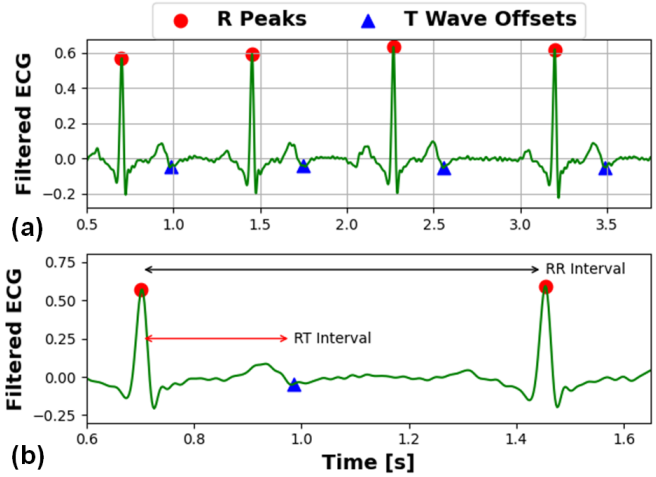

Fig. 3. (a) Detected ECG fiducial points (R peaks and T Wave offsets) and (b) corresponding time intervals (RR and RT intervals).

C. *Quotient based cardiac cycle description*

Having in mind available characteristic fiducial points a cardiac cycle can be described using a quotient based on RR and RT intervals. In this paper, quotient noted as r can be defined as:

$$r = \frac{RR - RT}{RT} \sim \phi \,. \tag{5}$$

This quotient can be find in the literature as the ratio of the diastolic and systolic phases of a cardiac cycle, where it is further averaged at the level of the cardiac cycle [13]. Moreover, RR interval can be expressed as a function of RT interval by applying the quotient:

$$RR = RT \cdot (1 + r) \,. \tag{6}$$

In that case the slope is equal to the value of the ratio increased by one, and can be used as a mathematical model of cardiac behavior.

D. *Statistical evaluation of the quotient based cardiac cycle description*

For each set of points a well known linear regression is performed and the direction coefficient, noted as k, is estimated. Also, for each coefficient calculated in this way, the relative error is estimated, and the value $1 + \phi$ is taken as the correct value. The error value is calculated based on the formula:

$$\delta = \frac{r - \phi}{\phi} \cdot 100\% = \frac{k - 1 - \phi}{\phi} \cdot 100\% \tag{7}$$

where constant in the proportion of the golden section is taken as the reference value ϕ [14]. In this case, the modified relative error stores information about the sign of deviation from the golden ratio. The value of the quotient r and the line direction coefficient obtained by linear regression are connected by a unique connection. Since there are several signals per each volunteer, in the second step averaging of the quotient values for a volunteer from the ECG ID database is performed.

IV. Results

Analysis was performed for signals from ECG ID database. After the described preprocessing, the detection of characteristic points and determination of RR and RT intervals for each cardiac cycle was performed. For each volunteer, ECG signals were recorded in several iterations meaning data was collected for a patient several times independently. Each calculated duration of RR and RT interval within a cycle make an ordered pair (RT, RR) representing a point in the RT-RR diagram. Figure 4 shows a set of all points for one volunteer from the ECG ID database, with all values observed for heart cycles from all iterations of signal recording as a single set. A linear regression procedure was performed on the set while forcing the passage of the regression line through zero (fit intercept is zero). As a result of linear regression, the direction coefficient k was obtained, which is equal to $1 + r$ on the basis of (6). This value is compared to a value of $1 + \phi$ where the constant ϕ corresponds to the golden ratio. The relative error in this case of the golden ratio is 1.14%.

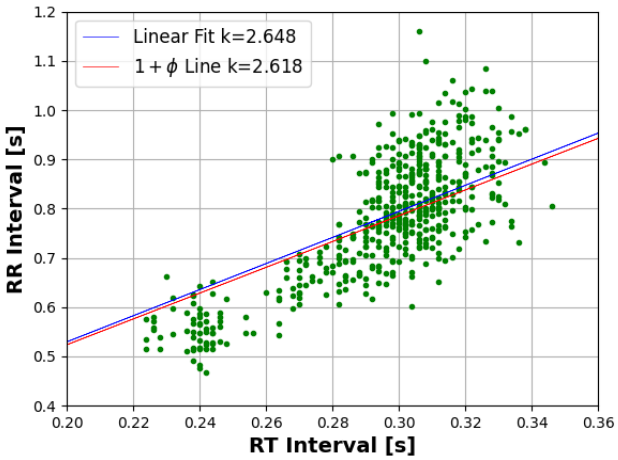

Fig. 4. Linear regression over points whose coordinates represent RR and RT values of cardiac cycles corresponding to a patient from ECG ID dataset.

In the second step, the quotient r is averaged after iteration for the same volunteer. In this way, each iteration corresponds to one ratio of the averaged quotient. Figure 5 shows histogram of the averaged values of the quotient r. The histogram was fitted according to the Gaussian distribution, and the parameters μ and σ were determined, which correspond to mean value and standard deviation, respectively. By comparing the mean value with respect to the value of ϕ, a relative error value of 2.35% was obtained.

The procedure that involves determining the set in the RT-RR plane was repeated for volunteers. In Fig. 6 several

 ISBN 978-86-7466-930-3

individuals from the ECG ID database (two males and two females) are shown through corresponding sets.

After the calculation of error values, it can be noted that for males negative values are obtained, while for females this value is positive. There has also been some separation in terms of points belonging to different volunteers, which means that it is possible to differentiate individuals of different sex to some extent on the basis of quotient calculation. In the experimental analysis this is obtained for around 80% cases of samples that belong to female volunteers and around 70% cases belonging to male individuals. This can be considered to be a good starting point for further research.

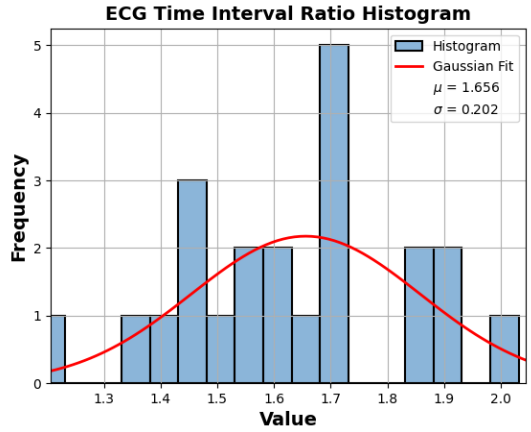

Fig. 5. Histogram representation and fitted normal distribution for averaged ratio values for a volunteer from the ECG ID database.

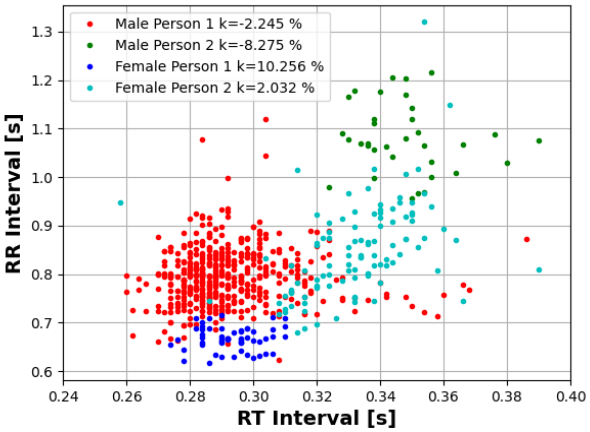

Fig. 6. Calculated RT and RR values in RT-RR domain for several volunteers.

V. Conclusion

In this paper, the analysis of cardiac cycles is performed through the consideration of a relationship that exists between RR and RT intervals. The linear regression procedure used to estimate the direction coefficient, describes the proportionality between two quantities quite well. The estimated direction coefficients are related to the corresponding quotient of the diastolic and systolic portions in ECG signal. Errors of the coefficient deviation from the reference constant are calculated and here, for healthy individuals, the results showed minimal deviations. Also, signals belonging to volunteers of different sex are observed in order to analyze the usefullness of the quotient. It is noticed in the experimental analysis that the error values between the calculated quotient and the "golden ratio" have common case of different signs depending on the gender.

This paper is an initial study to test the hypothesis of whether the corresponding relationships within the ECG signal follow the "golden ratio" for further use and experiments. In the next steps, it is necessary to analyze the bases on a wider scale, where we would also analyze the signals that are pathologically altered due to cardiovascular diseases.

Acknowledgment

This work is written during the research supported by the Ministry of Education, Science and Technological Development, Republic of Serbia, No. 2022/200103, and supported by the Academy of Technical and Art Applied Studies Belgrade, Department School of Information and Communication Technologies.

References

[1] J. D. Pollock and A. N. Makaryus, "Physiology, Cardiac Cycle," *StatPearls*, Oct. 2021, Accessed: Apr. 14, 2022. [Online]. Available: https://www.ncbi.nlm.nih.gov/books/NBK459327/.

[2] T. Waselius, J. Wikgren, H. Halkola, M. Penttonen, and M. S. Nokia, "Learning by heart: Cardiac cycle reveals an effective time window for learning," *J. Neurophysiol.*, vol. 120, no. 2, pp. 830–838, Aug. 2018, doi:10.1152/JN.00128.2018/ASSET/IMAGES/LARGE/Z9K0071846710007.JPEG.

[3] C. Ciucurel, L. Georgescu, and E. I. Iconaru, "ECG response to submaximal exercise from the perspective of Golden Ratio harmonic rhythm," *Biomed. Signal Process. Control*, vol. 40, pp. 156–162, Feb. 2018, doi: 10.1016/J.BSPC.2017.09.018.

[4] I. Ilić, M. Stefanović, and D. Sadiković, "MATHEMATICAL DETERMINATION IN NATURE-THE GOLDEN RATIO," doi: 10.5633/amm.2018.0317.

[5] W. T. Dobrosielski, J. Szczepański, and H. Zarzycki, "A Proposal for a Method of Defuzzification Based on the Golden Ratio—GR," *Adv. Intell. Syst. Comput.*, vol. 401, pp. 75–84, 2016, doi: 10.1007/978-3-319-26211-6_7.

[6] A. L. Goldberger *et al.*, "PhysioBank, PhysioToolkit, and PhysioNet," *Circulation*, vol. 101, no. 23, Jun. 2000, doi: 10.1161/01.CIR.101.23.E215.

[7] ECG database, "ECG-ID Database v1.0.0." https://physionet.org/content/ecgiddb/1.0.0/ (accessed Apr. 10, 2022).

[8] D. Makowski *et al.*, "NeuroKit2: A Python toolbox for neurophysiological signal processing," *Behav. Res. Methods*, vol. 53, no. 4, pp. 1689–1696, Aug. 2021, doi: 10.3758/S13428-020-01516-Y/TABLES/3.

[9] A. Rashkovska, and V. Avbelj, "Signal processing methods for ST variability assessment in ECG," In *2013 36th International Convention on Information and Communication Technology, Electronics and Microelectronics (MIPRO)*, pp. 331-334, IEEE, 2013. https://ieeexplore.ieee.org/document/6596277 (accessed Apr. 12, 2022).

[10] C. Li, C. Zheng, and C. Tai, "Detection of ECG characteristic points using wavelet transforms," *IEEE Trans. Biomed. Eng.*, vol. 42, no. 1, pp. 21–28, 1995, doi: 10.1109/10.362922.

[11] L. Maršánová *et al.*, "ECG features and methods for automatic classification of ventricular premature and ischemic heartbeats: A comprehensive experimental study," *Sci. Rep.*, vol. 7, no. 1, Dec. 2017, doi: 10.1038/S41598-017-10942-6.

[12] J. P. Martínez, R. Almeida, S. Olmos, A. P. Rocha, and P. Laguna, "A Wavelet-Based ECG Delineator Evaluation on Standard Databases," *IEEE Trans. Biomed. Eng.*, vol. 51, no. 4, pp. 570–581, Apr. 2004, doi: 10.1109/TBME.2003.821031.

[13] M. Ibranovic and A. Omerbasic, "View of The Human Heart: Deviating from the Golden Ratio and Diagnosing Disease," *American Academic Scientific Research Journal for Engineering, Technology, and Sciences*, *80*(1), pp. 73-79, 2021. https://asrjetsjournal.org/index.php/American_Scientific_Journal/article/view/6889/2415 (accessed Apr. 10, 2022).

[14] C. J. Kat and P. S. Els, "Validation metric based on relative error," *Mathematical and Computer Modelling of Dynamical Systems*, vol. 18, no. 5, pp. 487–520, Oct. 2012, doi: 10.1080/13873954.2012.663392.

Application of Bayes and knn classifiers in tumor detection from brain MRI images

Marta Mirkov and Ana Gavrovska, *Member, IEEE*

***Abstract*— Automatic detection of regions of interest is of great importance in computer-aided diagnosis systems. Magnetic Resonance Imaging (MRI) of head due to good soft-tissue contrast is widely used for brain tumor detection showing potential anomalies that indicate the need for further treatment. Current algorithms for processing and classification of medical images often involve complex designs of deep learning that require significant hardware resources and considerable execution time in order to assist doctors in detecting diseases. This may lead to labeling more complex cases in brain tumor detection. In this paper, statistical features are considered with application of Bayes and kNN classifiers showing comparable results having in mind publicly available brain tumor detection database.**

***Index Terms*— Magnetic Resonance Imaging, brain tumor detection, segmentation, feature extraction, machine learning.**

I. Introduction

Today, depending on the need, various medical imaging modalities are used: X-ray, fluoroscopes, mammography, computer tomography (CT) devices as well as devices based on nuclear medicine techniques – Positron Emission Tomography (PET) and Single Photon Emission Tomography (SPECT). However, equipment that does not require ionizing radiation can be used for computer-aided diagnosis systems. Magnetic Resonance Imaging (MRI) scanners employ strong magnetic fields and magnetic field gradients to generate images of the organs or the whole body, and are found very useful in diagnostics. For example, according to the World Health Organization (WHO), cancer is the second leading cause of death [1]. Cancer detection from biopsy procedures is a painful process for patients, and therefore appropriate medical imaging modalities can facilitate this procedure [2].

Images obtained from MRI scanners show satisfying soft-tissue contrast, which is suitable for brain imaging. They provide a good visualization of the posterior cranial fossa, which contains the brain stem and cerebellum. The contrast between gray and white matter makes MRI the best choice for diagnosing many central nervous system conditions, including demyelinating diseases, dementia, cerebrovascular disease, infectious disease, Alzheimer's disease, and epilepsy [3]. Since many images are taken in milliseconds, it shows how the brain reacts to different stimuli, thus enabling doctors to study the brain's functional and structural abnormalities.

In this paper, statistical feature extraction and application of two classifiers will be observed, where the aim is to create a simple algorithm for brain tumor detection [4]-[9]. One of the motivations is usefulness of texture related features in MRI images [10]. Also, one of the famous examples of hypothesis testing is the Bayes test [5], which will be implemented here, and compared to knn (k-nearest neighbors) approach [7] based on revising hand-crafted statistical features.

The paper is organized as follows. After the introduction, in Section II related work is presented. It considers traditional statistical feature extraction and machine learning usage in brain tumor detection. Steps in the experimental analysis performed in this paper are explained in Section III, where further details for feature extraction are given in Section IV. Section V is dedicated to classifiers design and performance evaluation. Obtained results and conclusion are given in Section VI and Section VII, respectively.

II. Related work

The brain tumor is an abnormal growth of cancer cells in the brain which disrupts the work of functional cells. Early detection and rapid diagnosis of tumors can help save the patient's life. Mathematical and software tools can be very successful in detecting brain abnormalities. Thus, related work is oriented towards statistical feature extraction and machine learning methods used in brain tumor detection.

Statistical features are found useful in machine learning and medical image segmentation and classification [10]-[12]. Particularly, in brain tumor detection texture is one of the most valuable features in designating the image appearance [10], [13]. It can be described statistically for the purpose of distinguishing image characteristics by the spatial allotment of gray levels. The most popular mathematical representation of image texture is co-occurrence matrix. For example, in the Gray Level Co-occurrence Matrix (GLCM), the spatial relationship of pixels is considered to examine the texture by using statistical methods. Four features can be extracted and found useful as in [10], [13]-[14]: energy, correlation, contrast, homogeneity. Namely, these features are used for extracting features and forwarding it to neuro-fuzzy models and, generally, machine and deep learning methods [15]-[18]. In [13] support vector machines are applied as classifier, where in [18] authors implemented deep convolutional neural network, and one of the publicly available datasets for brain tumor detection [19]. Using hand-crafted features are still valuable for obtaining satisfying results in brain tumor detection and more parameters may give better results. On the other hand, smaller dimension of the feature vector is important for algorithm execution, especially in the cases

Marta Mirkov is with the University of Belgrade - School of Electrical Engineering, Bulevar kralja Aleksandra 73, 11120 Belgrade, Serbia (e-mail: marta.mirkov@gmail.com).

Ana Gavrovska is with the University of Belgrade - School of Electrical Engineering, Bulevar kralja Aleksandra 73, 11120 Belgrade, Serbia (e-mails: anaga777@gmail.com ; anaga777@etf.rs).

 ISBN 978-86-7466-930-3

where there is no need for higher complexity according to tested dataset. In this paper, Bayes and knn classifier are analyzed for classification model implementation using [19].

III. Experimental analysis

The cancer tissue is expected to stand out from the normal part of image, but the question of choice of MRI features still remains. The experimental analysis performed here consists of:

- tumor segmentation based on labeled regions in images,
- hand-crafted feature extraction,
- classification and evaluation of results on available dataset.

The proposed work is tested with Brain MRI Images for Brain Tumor Detection dataset [19], containing 98 brain MRI images with healthy tissue and 155 brain MRI images with cancer tissue. Among features for segmentation task solidity of labeled regions is applied. Having in mind traditional hand-crafted features for classification: energy, correlation, contrast and homogeneity, two classifiers are tested in initial phase. Based on preliminary segmentation analysis, two additional statistical features are added for the binary classification. Both tested classifiers, Bayes and knn, are evaluated on the test set, which is made from 30 % of the whole dataset selected in a random manner, where the rest was used for the training set. For performance evaluation true positive rate (TPR), true negative rate (TNR) and balanced accuracy (BACC) are calculated as in (1)-(3), respectively:

1) *True Positive Rate- TPR*

$$Sensitivity = \frac{TP}{P}, \quad (1)$$

where TP represents true positive, the number of samples that were positive and detected as positive, and P represents the whole set of positive samples;

2) *True Negative Rate- TNR*

$$Specificity = \frac{TN}{N}, \quad (2)$$

where TN represents true negative, the number of samples that were negative and detected as negative, and N represents the whole set of negative samples;

3) *Balanced Accuracy- BACC*

$$BACC = \frac{TPR + TNR}{2}. \quad (3)$$

IV. Proposed tumor segmentation

Proposed brain tumor segmentation is consisted of several steps. Firstly, MRI image is preprocessed using: high-pass filtering and image intensity adjustment, and then, after image binarization, connected regions are labeled. Finally, solidity is implemented for tumor segmentation.

A. MRI image preprocessing and labeling

High-frequency filtering highlights sudden changes in the image by passing high-frequency components [4]. A fifth order Gaussian HP filter with cutoff frequency of 55 Hz was used. Although MRI images provide good tissue contrast, adjusting image intensity is important for tumor segmentation. By saturating the bottom 2% and the top 1% of all pixel values the grayscale range of image is shortened and the contrast is enhanced, and therefore it highlights tumor areas.

Because the image contrast is adjusted, the histogram of the image has a bimodal distribution with a deep and sharp valley between the two peaks, which enabled using Otsu's method for automatic thresholding [4]. Finally, binary image has different white regions where some of them might represent tumor tissue. Pixels are connected and are part of one region if their edges touch. Two adjacent pixels are part of the same object if they are both of the same intensity and are connected along all directions.

B. Solidity characterization

For each labeled region, solidity can be calculated. Solidity is a measurement of the overall concavity of a particle. It is defined as the image area divided by the convex hull area. As the object form digresses from a closed circle, the convex hull area increases, and the calculated solidity decreases. Images with high solidity are more likely to contain tumor regions [13, 23]. A tumor can successfully be detected by comparing the calculated solidity of the labeled image with a higher value (closer to 1). In this case, the tumor is detected if solidity is higher than 0.6. When this area represents a tumor, it is the region or candidate with more white pixels, and when there is no tumor tissue on the image, some small regions can still be extracted. It may be assumed that differences between healthy and tumor tissue can be provided using features that describe the area and shape of this extracted region.

V. Statistical hand-crafted features

GLCM is created by calculating how often a pixel with grayscale intensity value i occurs horizontally adjacent to a pixel with the value j. Offset isn't used for defining pixel spatial relationships. The number of gray levels in the image determines the size of the GLCM. Scaling to 8 gray levels is used to reduce the number of intensity values in an image, so the size of GLCM is 8x8 pixels. The traditional statistical hand-crafted features extracted from GLCM are: energy, correlation value, contrast and homogeneity.

Energy estimates the sum of squared elements from GLCM and represents feature 1:

$$Energy = \sum_{i,j=0}^{N-1} p^2(i,j), \quad (4)$$

where N represents the number of pixels in image, i and j the location of pixel, and $p\,(i,j)$ the intensity of the pixel at the location (i,j).

The mentioned pixel pairs are then estimated using joint probabilities. It gives linear dependency of the gray levels of neighboring pixels. In general, it ranges from [-1,1]:

$$Correlation = \sum_{i,j=0}^{N-1} \frac{(i-\mu x)(j-\mu y)p(i,j)}{\sigma_x \sigma_y}, \quad (5)$$

where μ_x, μ_y, are the means and σ_x and σ_y are the standard deviations of P_x and P_y, respectively. Note that $P_x(i)$ is the ith entry in the marginal-probability matrix obtained by summing the rows of $P(i, j)$ and $P_y(i)$ is the ith entry in the marginal-probability matrix obtained by summing the rows of $P(i, j)$.

Contrast value (feature 3) estimates the local variations, i.e. sum of square variance, as in (6):

$$Contrast = \sum_{i,j=0}^{N-1} |i-j|^2\, p(i,j). \quad (6)$$

The fourth feature, homogeneity, estimates the closeness of distributed pixels.

 ISBN 978-86-7466-930-3

$$Homogenity = \sum_{i,j=0}^{N-1} \frac{p(i,j)}{1+|i-j|}. \quad (7)$$

These four features are applied in brain tumor detection, but having in mind the segmentation task, in combination with two more features like the number of white pixels (feature 5) and skewness (feature 6), one may assume further improvements can be obtained. The number of white pixels in the segmented images are expected to increase the accuracy results. Also, some additional statistical parameters can be great indicators of tissue condition. Skewness represents a measure of the asymmetry of the probability distribution [20]. It can be expected that umor tissue has much higher skewness than healthy tissue, thus it is also a reliable feature for classification.

VI. Bayes and knn Classifiers and Evaluation of the Results

A. Bayes classifier

For implementing Bayes classifier, it is necessary to define the posterior probabilities $q_i(X)$ which represent the conditional probability that the sample X comes from the class ω_1 if its exact realization is known. Using the Bayes theorem, these probabilities can be calculated if priori probabilities of occurrence of class p_i and posterior density probability functions of measured vectors $q_i(X)$ are known [5], [11]. In this case, the first class represents images with tumor tissue, and the second represents healthy tissue. A simple decision rule can be made based on conditional probabilities:

$$q_1(X) > q_2(X) \Rightarrow X \in \omega_1 \quad (8)$$

$$q_2(X) > q_1(X) \Rightarrow X \in \omega_2 \quad (9)$$

Although the probability density functions of the classes are not known, it can be assumed that, if there is a large number of samples, they can be taken as Gaussian (according to the central limit theorem) [6]:

$$f(x) = \frac{1}{|\Sigma|^{1/2}(2\pi)^{n/2}} e^{-(X-M)^T \Sigma^{-1}(X-M)} \quad (10)$$

where n represents the dimension of the vector X, M the mathematical expectation of the vector X, and Σ the covariance matrix of the feature vector. These values for both classes are obtained from the training set. For both classes, feature vectors are formed for classification.

B. k nearest neighbors Classifier

The most common issue in practice is information missing needed for classification based on hypothesis testing, so one may resort to non-parametric classification. One of the most popular methods is k nearest neighbors or knn. The algorithm classifies the observation point in relation to how the neighbors are classified. In the knn algorithm, k is a parameter that indicates the number of nearest samples involved in the classification [7], [21].

In Fig. 1, a new green sample that needs to be classified can be observed. The full circle in the figure represents the case when k=3: the neighbors are one blue square and two red triangles. Since there are more triangles, the green circle sample is assigned to the same class as the triangles.

However, if four is taken for k, the green circle will be classified into the blue squares class because there are more of them in the region. In conclusion, k is an essential parameter for successful classification [21]. Also, the success of the classification depends on which methods are used for defining what the nearest neighbors are. Some of the methods that are going to be considered in this paper are Euclidean, Chebyshev, Mahalanobis distance, and cosine similarity [22].

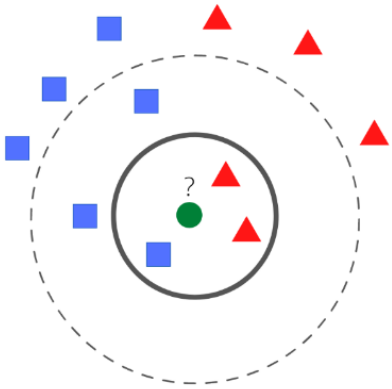

Fig. 1. Graphical representation of knn method, where green circle sample needs to be assigned to blue rectangle or red triangle class.

C. Evaluation

On proposed tumor segmentation steps and feature extraction, results of Bayes and knn classifiers will be shown, as well as the influence of feature vector dimension on results. The performance will be evaluated using confusion matrices and metrics described by (1)-(3).

The confusion matrix for this classification consists of two columns and two rows. Each row of the matrix represents the instances in an actual class, while each column represents the instances in a predicted class. Images with tumor tissue are labeled as ‘positive’, and healthy tissues are labeled as ‘negative’. Four and six features are tested to observe the effects on the results using Bayes and knn classifiers. The effect of the distance type and different values of k (1 to 40) on accuracy have been also analyzed.

VII. Experimental Results

A. Preliminary segmentation and feature inspection results

Preliminary segmentation results are show in Fig. 2 and Fig. 3. It can be observed that tumor is correctly detected in Fig. 2 for cancer tissue example. In the image with healthy tissue in Fig.3, small regions which are not tumor are segmented as one (false) candidate. Segmented image that contains a tumor has larger white area extracted, as it can be seen in Fig. 2 and Fig. 3, so this can be also used as an effective feature that provides good separability.

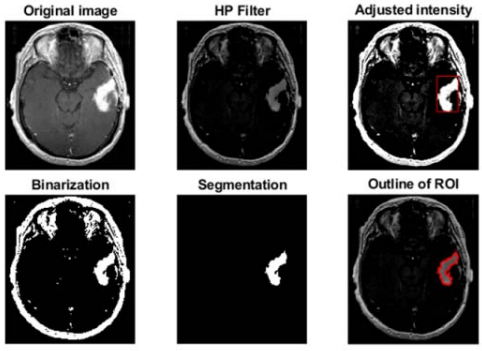

Fig.2. Results of segmentation for cancer tissue

 ISBN 978-86-7466-930-3

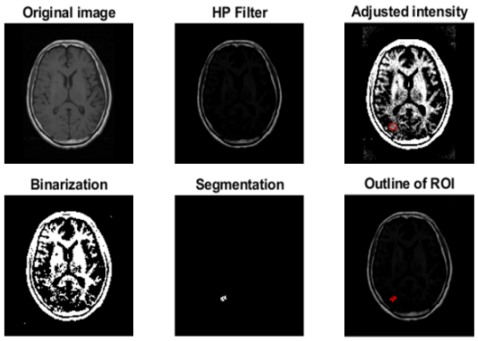

Fig. 3. Results of segmentation for normal tissue

Using the first four hand-crafted features may not be enough for high accuracy results. Adding two more features (feature 5 and feature 6) can improve results. From Fig.3 some of the separability inspection results can be seen.

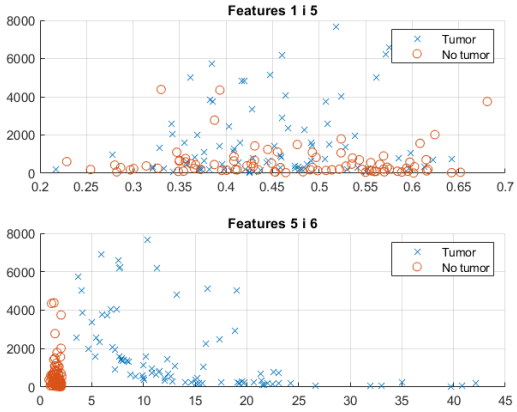

Fig. 4. Some of the separability inspection results of the selected features.

B. *Classification results using proposed method*

Classification results with only traditional or texture related features using Bayes classifier did not give expected results, as presented in Table I. Similarly is obtained for knn classifier and it is presented in Table II. For higher accuracy results, these classifiers require more information obtained through using additional features.

TABLE I
RESULTS OBTAINED WITH BAYES CLASSIFIER

Metric	TPR	TNR	BACC
Traditional four feature approach	71.4 %	82.6 %	75.8 %
The proposed method	96.6 %	100 %	98.3 %

TABLE II
RESULTS OBTAINED WITH KNN CLASSIFIER

Metric	TPR	TNR	BACC
Traditional four feature approach	89.6 %	65.5 %	77.6 %
The proposed method	100 %	96.5%	98.2 %

In the case of knn and four feature selection, the accuracy is highest for the Chebyshev distance, which is achieved for k = 39. This is illustrated in Fig. 5. These results are not suitable for practice and two additional features are applied to feature vector. The accuracy in the case with more features is highest for the cosine similarity and the best case is secured with lower number of neighbours (k = 3), which can be seen in Fig. 6, where smaller number of neighbours is a better choice.

For medical image classification, sensitivity is aimed to be high because of the need for all positives to be recognized correctly. Specificity should not be low because many false alarms are undesirable.

It is proven that only four texture related features cannot provide expected results, and adding two more features improves results. Feature vector still contains relatively small number of elements. In further experiments it is shown that the kNN algorithm with more features provides reliable results for all parameters, and compared to the Bayes classifier, it provides better sensitivity for both cases (with the lower and higher number of features), which can be seen in Table III. Slightly higher results in overall evaluation are obtained for knn for the proposed method.

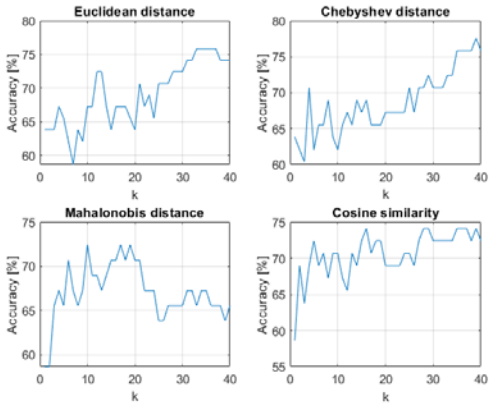

Fig. 5. Accuracy versus parameter k for four types of distances for four feature approach.

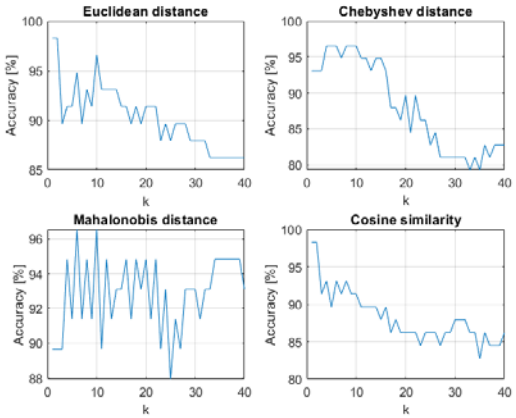

Fig. 6. Accuracy versus parameter k for four types of distances for proposed approach.

VIII. CONCLUSION

The proposed tumor segmentation in MRI head images provided an excellent base for analyzing the tumor classification methods. The proposed classification method gives surprisingly good results compared to the other methods based on machine learning tested on the same dataset. The advantage of the proposed method lies in less demanding hardware resources where traditional classification methods are used. A more diverse selection of features can further increase accuracy. Since the knn method stood out as a method with high accuracy, it is possible to test other selections and analyze the types of distances by

 ISBN 978-86-7466-930-3

which the classification is performed.

A possible improvement of the model would also be classifying different types of tumors and labeling more complex cases in brain tumor detection. Such data labeling for classification improvements would require help from the experts.

ACKNOWLEDGMENT

This work is written during the research supported and partially funded by the Ministry of Education, Science and Technological Development, Republic of Serbia. No. 2022/200103.

REFERENCES

[1] H. Ritchie and M. Roser, "Causes of Death," Published online at OurWorldInData.org. Retrieved from: 'https://ourworldindata.org/causes-of-death', 2018.

[2] S. Webb, *The physics of medical imaging*, Taylor and Francis Group, Country: USA, 1988. https://doi.org/10.1201/9780367805838

[3] R.A. Sadek, "An improved MRI segmentation for atrophy assessment," *International Journal of Computer Science Issues* (IJCSI) vol. 9, no. 3, pp. 569-574, 2012.

[4] M. Popović, *Digitalna obrada slike,* Akademska misao, Serbia, 2006.

[5] B. Efron, "Bayes' theorem in the 21st century," *Science*, vol. 340, no. 6137, pp. 1177-1178, 2013.

[6] S.G. Kwak, and J.H. Kim, "Central limit theorem: the cornerstone of modern statistics," *Korean journal of anesthesiology*, vol. 70, no. 2, pp. 144-156, 2017.

[7] G. Guo, H. Wang, D. Bell, Y. Bi, and K. Greer, "Knn model-based approach in classification," OTM Confederated International Conferences "On the Move to Meaningful Internet Systems," pp. 986-996, 2003. Springer, Berlin, Heidelberg.

[8] S. A. Medjahed, "A comparative study of feature extraction methods in images classification," *International journal of image, graphics and signal processing* vol. 7, no. 3, pp. 16-23, 2015.

[9] P. Nair, and I. Nair, "Classification of medical image data using k nearest neighbor and finding the optimal k value," *International journal of scientific & technology research*, vol. 9, no. 4, pp. 221-226, 2020.

[10] P.K. Bhagat, P. Choudhary, and K.M. Singh, "A comparative study for brain tumor detection in MRI images using texture features," Chapter 13: In Advances in ubiquitous sensing applications for healthcare, *Sensors for Health Monitoring*, Academic Press, vol. 5, pp. 259-287, 2019. https://doi.org/10.1016/B978-0-12-819361-7.00013-0

[11] K. Fukunaga, *Introduction to statistical pattern recognition*, (2nd ed.), Academic Press Professional, Inc., USA. 1990.

[12] J. Jaidip, N. Patil, C. Kala, K. Pandey, A. Agarwal and A. Pradhan. "Statistical characterization of tissue images for detection and classification of cervical precancers." arXiv preprint arXiv:1112.4298 2011.

[13] K. K. Kumar, M. Devi T, and S. Maheswaran "An Efficient Method for Brain Tumor Detection Using Texture Features and SVM Classifier in MR Images*." Asian Pacific journal of cancer prevention* :APJCP vol. 19, pp. 2789-2794, 26 Oct. 2018, doi: 10.22034/APJCP.2018.19.10.2789

[14] M. Domingo, and D. Filbert. "Classification of potential defects in automated inspection of aluminium castings using statistical pattern recognition," *8th European Conference on Non-Destructive Testing* (ECNDT 2002), pp.1-10, 2002.

[15] T.M. Hsieh, Y. M. Liu, CC Liao, F. Xiao, I-J. Chiang, J-M. Wong, "Automatic segmentation of meningioma from non-contrasted brain MRI integrating fuzzy clustering and region growing", BMC Med Inform Decis Mak 11, 54, 2011. https://doi.org/10.1186/1472-6947-11-54

[16] K. Sharma, A. Kaur, and S. Gujral, "Brain tumor detection based on machine learning algorithms," *International Journal of Computer Applications* 103.1, pp. 7-11, 2014.

[17] R. Ranjbarzadeh, B. Kasgari, S. J. Ghoushchi, S. Anari, M. Naseri, M. Bendechache, "Brain tumor segmentation based on deep learning and an attention mechanism using MRI multi-modalities brain images", Sci Rep 11, 10930, 2021. https://doi.org/10.1038/s41598-021-90428-8

[18] A. Çinar, and M. Yildirim, "Detection of tumors on brain MRI images using the hybrid convolutional neural network architecture," *Medical hypotheses*, *139*, 109684, 2020.

[19] Brain MRI images for brain tumor detection dataset: https://www.kaggle.com/navoneel/brain-mri-images-for-brain-tumor-detection

[20] H. J. Baek, H. S. Kim, N. Kim, Y. J. Choi, Y. J. Kim. "Percent change of perfusion skewness and kurtosis: a potential imaging biomarker for early treatment response in patients with newly diagnosed glioblastomas." *Radiology* vol. 264, no. 3, pp. 834-843, 2012.

[21] I. K. Preeti Nair, "Classification of medical image data using k nearest neighbor and finding the optimal k value," *International journal of scientific technology*, volume 9, 2020.

[22] R. Ehsani, and F. Drabløs, "Robust Distance Measures for k NN Classification of Cancer Data," *Cancer informatics*, *19*, 1176935120965542, 2020.

[23] M. A. Javid, S. A. Buzdar, "A novel computer aided diagnostic system for quantification of metabolites in brain cancer," *Biomedical Signal Processing and Control*, Volume 66,102401, 2021. https://doi.org/10.1016/j.bspc.2020.102401

From puppet-master creation to false detection

Ana Pantelić and Ana Gavrovska, *Member, IEEE*

***Abstract*— Nowadays, many issues in society are affected by the misuse of deepfakes. One can say that we came to a point when prior knowledge of image processing is not a requirement for deepfake creation. With different motives, in a short period, and with limited resources, many deepfakes can appear on the internet. That brings us to testing that hypothesis of how easy and how fast someone can make a deepfake. In this paper several puppet-master creations are made for experimental purposes. In the aftermath of deepfake creation, an off-shelf available deepfake detection algorithm is applied for the detection analysis which is expected not to be universal solution for every type of deepfake realization. This brings us to high false detection, where specific cases are considered in this paper, like closed eye and head shape effects.**

***Index Terms*— Deepfake, puppet-master, deep learning, closed eye, head shape, false detection.**

I. INTRODUCTION

Technologies are rapidly evolving, and the challenges due to hardware limitation are becoming obsoleted. On the other side, different associations are trying to solve technical issues through hackathons with solutions in the interest of society. One of those issues is the detection of deepfakes [1]-[3].

DeepFakes are getting easier to produce and harder to detect. DeepFake can be considered as altering approach based on artificial intelligence and deep learning architecture. Moreover, there are different types of deepfakes, where deepfake can be often described as a synthetic switch of identities of two persons, for example in a video sequence. Namely, there are different types of deepfakes like: face-swap, entire face synthesis, puppet-mastery, and lip-syncing [4]. It is highly used in revenge pornography, and based on DEEPTRACE research [5]-[6], in September 2019, 96% of deepfake videos belong to pornographic content, where the victims are widely women. There are also widely used for politicians and public figures. With available software tool almost everyone can generate a deepfake or deepface using recorded video and an image of a taget person.

In this paper a puppet-master creation as a popular method for deepfake creation is applied. Here, performed steps for creating a deepfake is explained. Moreover, one of the methods for deepfake detection is implemented in order to observe false detections. One may have in mind that the algorithm taken for experimental analysis is not selected purposely, but in a random manner from available recent solutions, in order to observe expected false detections. It is to expect that the detection method is not prepared for dealing with each type of deepfakes and scenarios. Thus, the motivation of this work is to perform popular deepfake generation and observe what would happen if a deepfake creation approach is not directly connected to some of the state-of-the art solutions focusing on specific details like edges around important face parts like: mouth, eye and similar.

The paper is organized as follows. After introduction, in Section II we give a brief description of popular deepfake creation and detection. Section III is dedicated to simulations for puppet-master creation and for neural network based detection without taking into account the type of creation. This is followed by the experimental results and discussion related to observed detection results in Section IV. Final conclusions are given in Section V.

Ana Pantelić is with the University of Belgrade - School of Electrical Engineering, Bulevar kralja Aleksandra 73, 11120 Belgrade, Serbia (e-mail: anaapantelic@gmail.com).

Ana Gavrovska is with the University of Belgrade - School of Electrical Engineering, Bulevar kralja Aleksandra 73, 11120 Belgrade, Serbia (e-mails: anaga777@gmail.com; anaga777@etf.rs).

II. DEEPFAKE CREATION AND DETECTION

One of the most popular ways of creating deepfake is GAN (Generative Adversarial Network) [7]-[8]. GAN is an algorithm with two opposed neural networks that generate new, synthetic data that can pass as regular data. Neural networks and, generally, machine learning tools show the ability to mimic the human brain by learning, memorising and making the data they acquire in general. Typical deepfake algorithms for generating data are X2Face and First order motion model [2]-[3], [9].

In this paper, the neural network starts with the Monkey-Net neural network [10], and advance it to the First order motion model for image animation [9]. The First order motion model presents a fast and effective way of creating a deepfake with better results than advanced animation processing software.

Puppet-master deepfake creation is one of the modest and popular methods for making a deepfake. It shows how realistic the results can be, where the artefacts are still seen by human eye especially in video material. So, this method for creating a deepfake has its positive and negative sides. Artefacts are observable and this can be negative experience for the creater. This is also a positive information since we can still believe that we can distinguish true or false video story.

For deepfake detection, one has to be aware of the algorithm used for deepfake creation. Taking into consideration that the person who published a deepfake won't leave a piece of information related to origin or source or used tools for deepfake design, the common decision is that the detection from practial point of view will be applied to images cropped/grabbed from the video.

The main focus of detection of a deepfake are face parts like eyes and mouth, and head movement. Deepfake may be recognized on irregular pixel weight at the edges of the mentioned regions after training the neural network that detects them. One of the state-of-the art models based on such detection is Meso-4 model [11]-[12]. It is based on convolutional neural network and represents an efficient tool for dealing with particular types of visual modifications.

 ISBN 978-86-7466-930-3

Here, it is used as only one of the solutions for observing how can some deepfake examples created by the First order motion model be detectable as deepfakes and what are the cases when one may get high number of false detections, when deepfake frames are passed as regular images.

III. SIMULATION

A. *Steps for creating a deepfake*

Here, preparations for the deepfake creating is filming a video of 256×256 px, that is frontal with simple backround. Next to that, an image of a person we want to switch the identity with is chosen. The selected image is also frontal with simple backround and with the lack of face-covering details. In this paper Google Colaboratory with python script are used for experimental purposes [13]-[14].

First order motion model for image animation is upgraded convolutional neural network based on Monkey-Net-u [9], [11]. Monkey-Net codes information of movement through keypoints that are pretrained and self-observed. Down side of this neural network is possibly that, while following the trajectory of keypoints in faster movements, missing spots in image can appear. To solve that missing spot, affine transformation is used to perserve the propotion of the line and collinearity between dots. While it perserves propositions between lines and dots, affine transformation doesn't perserves all the angles. To have a clear overview, the improved parts of Monkey-Net are: keypoints aren't just detected but they are self-controled, which will add the adaptability on the targeted image; the generator of occlusion is added that gives a mask based on the parts that are not initially visible; it improved the visual domain of the puppet in general. In Fig. 1 simulation steps for creating a puppet deepfake are shown. If we follow from the video of the puppet, the keypoints are generated and local affine transformation is applied and collected. Until it comes to dense motion, from the source image we encode all the needed features and by warp operation the parts of process are connected. This is followed by occlusion map and decoder that brings the final creation result.

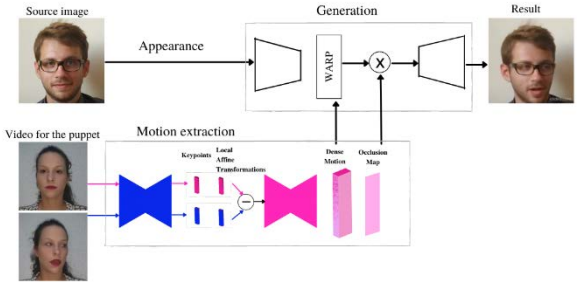

Fig. 1. Simulation steps for creating a puppet deepfake.

B. *A deepfake detection model*

For the need of deepfake detection, a pretrained convolutional neural metwork MESO-4 model is used [12]. The architecture of the model is shown in Fig. 2. It is constructed of four convolutional blocks and one hidden layer. It recognizes the vertical and horizontal lines; applies batch normalization; uses the convolutional matrix with a task to bring all the important edges like edge of the lips, shape of the head or edges of the eyes; it employs pooling layer that will pick the pixel with dominating characteristics. Based on the pixel the reducing of spatial size of convolutional operations is possible. To improve the generalization, in the addition to the normalization of the batch, ReLU (Rectified Linear Unit) which introduces nonlinearity is applied.

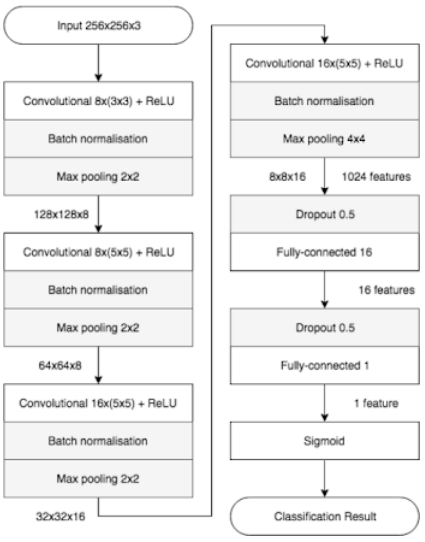

Fig. 2. Meso-4 architecture, where layers and parameters are displayed in rectangles [12].

C. *False detection counting in a puppet related data*

We wanted to see if the head movement and misshapes of the head will be detected by Meso-4 neural network. That is the reason we produced the video with head movement on both sides (left and right), and then abruptly moved to one of the sides. Furthermore, the idea is to make mouth and eyes to seem natural in a deepfake, so the person often blinks. When making mouth movements, the mouth is moved naturally without exaggeration.

IV. EXPERIMENTAL RESULTS

A. *Experimental results for created deepfakes and false detection*

Three deepfake videos are made with source images of university assistant, public figure, and politician. One of the created deepfakes for a public figure is shown in Fig. 3.

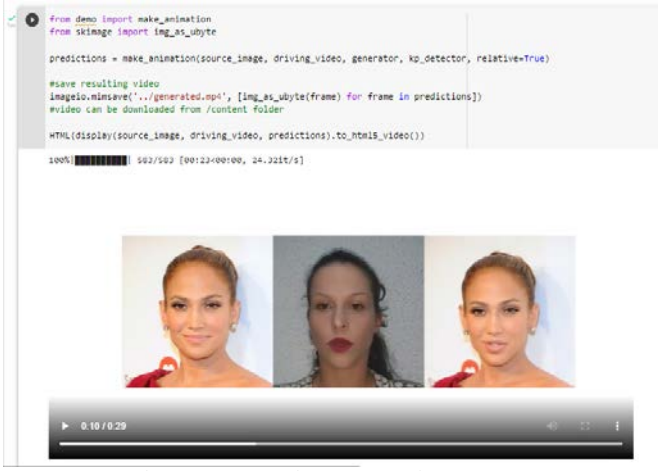

Fig. 3. One of the created deepfakes. From left we have source image, video for the puppet and the end result.

 ISBN 978-86-7466-930-3

The results were satisfying, with expected characteristics of puppet-mastery. The process resulted in a source image that was following all the given movements of head, eyes, and lips.

For the detection task both original and deepfake frames are used. Totally, 461 images are tested whether they are real or not, giving for original examples satisfying results as shown in Fig. 4. Predicted likelihood is close to 1 which means that labeling is performed in adequate manner. Correct prediction can be noticed and it proves that the result is true.

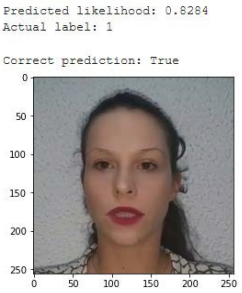

Fig. 4. The result of the detection. If the predicition is closer to one it means it sees it as real, and next to that it proves it predicition as True or False.

At first glance, a lot of images that are real are also detected as real, but unsatisfactory results are shown for deepfakes. The summary of obtained results is given in Fig.5. Out of 110 real images, 94 real cases are detected. On the other hand, high percentage is found for false detections where deepfake frame is considered real. In the experiment it is found that we have around 82.33% of chances for misinterpreting a deepfake image as real, and around of 14.5% of misinterpreting a real as a deepfake. The high false detection exists as it was expected.

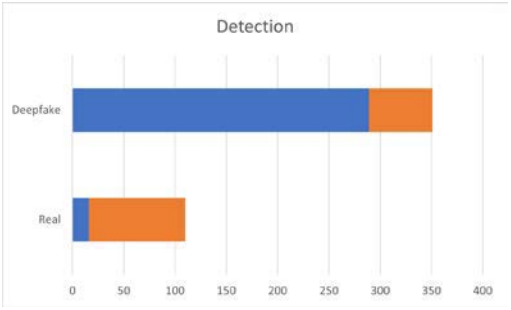

Fig. 5. The summary of detection. The blue colour presents the number of falsely detected images. Out of 351 deepfake images, 289 are detected real.

B. Further analysis on accurate results

When observing accurate real results it was noticed that the probability of images with closed eyes, and when the head is curved, is close to 0.5, which means that there is a significant level of doubt. Similarly is noticed with cases where errors occurred, i.e. when real images are detected as deepfakes. The probability of around 50% can be interpreted as random class selection.

In Fig. 6 examples of true predictions are presented, where one of the examples show lower predicted likelihood. This is the case where eyelids and pupils are not visible while blinking. On the other hand, when eyelids and pupils are visible and when there is less blur around the face, there is a higher probability that the detected image is real.

Fig. 6. Examples of True predicitions.

There are frames that are detected as deepfake and similar pattern can be recognized as in Fig. 7.

Fig. 7. Real images detected as deepfake

It can be noted that there are frames in Fig. 7. where pupils and irises are not visible, as well as where there is a greater curvature of the head. In these cases Meso-4 has detected that there is a chance that it is a deepfake. Also, it is important to note that most predictions are around 0.4 and that the probability leans towards deepfake, mostly where the eyes are closed and the head is tilted. The results of the experiment were best shown on the targeted personalities with similar facial symmetry as in the video used for the puppet.

The script for the puppet video had slow head movements to one side and then to the other, and then it abruptly moved to one side to see the artefact mentioned in the works for Monkey-Net and the First Order Motion Model. The appearance of this artefact was expected, and the artefact appeared in the results. For a better solution, photos from other angles should be found for the target person, which would improve the occlusion - in the sense that the focus is placed on the other eye (which should not be visible) or the whole part of the face that should be covered, and a 3D model, which is not obtained here due to the different shape of the person's head in the original. As for the background, the improved occlusion gave favourable results. Also, on several clippings, an artefact was obtained, which was conceptually mitigated, and that is the disappearance of parts of the image/person, as shown in Fig.8.

Fig. 8. Image with the disappeared part of the image

 ISBN 978-86-7466-930-3

Accurate results are obtained in this case, and a significant number of cases, as shown in Fig.9. It can be immediately noticed that the third of the displays are around 0.4 probabilities. All detected images have distorted heads and artefacts due to movement, i.e. tracking the trajectory of key points on the face of different symmetry in the 3D model or they have their eyes closed.

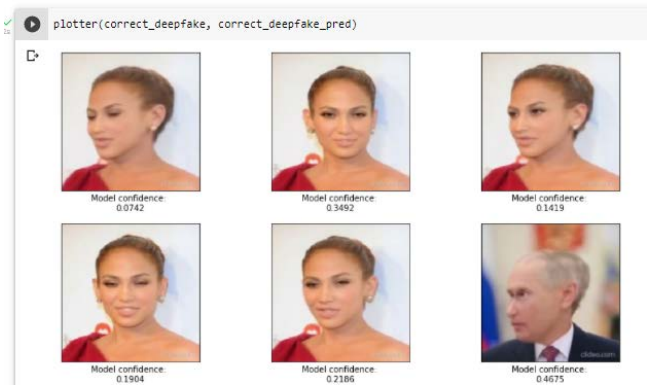

Fig. 9. Examples of images that are deepfakes, and detected as deepfakes

C. *Analysis of false detection results*

Here, of the greatest importance are images that are detected as real, and these are images from deepfake videos.

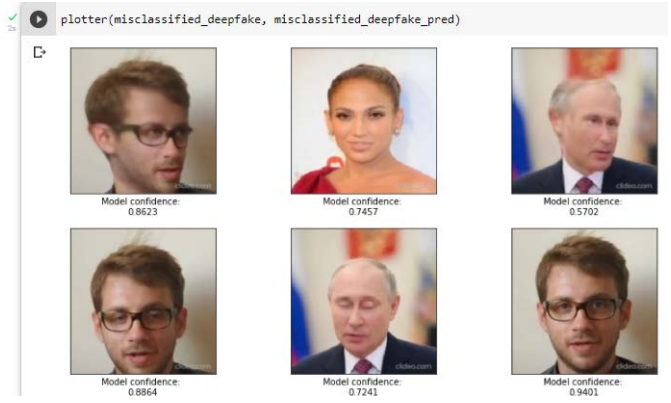

Fig. 10. Examples of images that are deepfakes and detected as real.

Three specific cases can be observed where there is a space for further improvements:
- mouth/lip movements,
- head movements and
- eye movements

Speaking of mouth movements, Fig.11, satisfactory results were obtained in creating a puppet, where the targeted persons followed the movements and had a tooth display at the appropriate moments. All lip movements that were observed in isolation from other movements contributed to the reality of deepfake and false detection. The lips are mostly in motion with teeth or collected. Compared to well-detected lips, every fifth well-detected mouth as a deepfake has a deformity along with the head. So one can say that lips are one of the parts where there is a need for a better detection.

Slow head movements to one side and then the other, and then abruptly movement to one side is a significant process, Fig.12. All the end movements are recognized as real images, in a manner that if the head is still, meaning in one place for more than one second without motion blur, the image will be detected as real. Furthermore, the detector sees even distinguished distortions of the head and face as realistic images. This is noticed in nearly 33% of false detected images. Moreover, it is very likely to have errors in differentiation when real images are frontal with clear head movement, while eyes are visible and lips in motion or collected. Those characteristics are visible in around 97% of all images that are deepfake and marked as real.

Fig. 11. Images with mouth movement

Fig. 12. Examples of frontal, right, left and right side (column-wise).

The most relevant results in terms of authenticity are in creating obtained by tracking eye movements, Fig.13. It can be considered the most difficult case in the creation process. False detection occurred in the eye related situations when the eyes are fully visible or when the iris and pupil are visible. Also, false detection is present when the eyes have a proportional distance between the pupils concerning the position of the face. This is shown in the most majority of images/frames, around 99%.

Fig. 12. Examples of eye movement.

 ISBN 978-86-7466-930-3

V. CONCLUSION

Based on the results of the experiments, it can be concluded that the creation of fast and efficient deepfake still meets the need for additional training of neural networks that map key points and where trajectories needs to be adapted to different head shapes so that the appearance of deepfake is invisible to the human eye. It is important to emphasize that the results completely coincided with the results from the paper [9]. It is believed that further training of such neural networks can lead to even more adaptable results.

On the other hand, the selected detection was not the best example for a given set of images which is shown through a variety of false detection results. This can be attributed to the fact that the detection follows certain edges and looks for dominant characteristics that were not the focus in creating the deepfake, such as eye details. Therefore, it is suggested that the type of detection should be adapted to specific type of deepfake. The importance of focusing on deepfake detection, and particularly eye movement, is emphasized which must be adapted to all new ways of creating deepfake videos.

In future work, we would focus on better detection of the misshaped head, as well as different tools for recognition of lip-syncing and eye tracking.

ACKNOWLEDGMENT

This work is written during the research supported and partially funded by the Ministry of Education, Science and Technological Development, Republic of Serbia. No. 2022/200103.

REFERENCES

[1] A.M. Almars, "Deepfakes detection techniques using deep learning: a survey," *Journal of Computer and Communications*, vol. 9, no. 5, pp. 20-35, May 2021.

[2] J.T. Hancock, and J.N. Bailenson, "The social impact of deepfakes," *Cyberpsychology, behavior, and social networking*, vol. 24, no. 3, pp. 149-152, 2021.

[3] M. Đorđević, M. Milivojević, and A. Gavrovska, "DeepFake video production and SIFT-based analysis," *Telfor Journal*, vol. 12, no. 1, pp. 22-27, 2020.

[4] M. Masood, M. Nawaz, K.M. Malik, A. Javed, and A. Irtaza, "Deepfakes Generation and Detection: State-of-the-art, open challenges, countermeasures, and way forward," *arXiv preprint arXiv:2103.00484*, 2021.

[5] C. Gosse, and J. Burkell, "Politics and porn: how news media characterizes problems presented by deepfakes," *Critical Studies in Media Communication*, vol. 37, no. 5, pp. 497-511, 2020.

[6] J.P. Dasilva, K.M. Ayerdi, and T.M. Galdospin, "Deepfakes on Twitter: Which Actors Control Their Spread?," *Media and Communication*, vol. 9, no. 1, p. 301-312, 2021.

[7] L. Guarnera, O. Giudice, and S. Battiato, "Deepfake detection by analyzing convolutional traces," In *Proceedings of the IEEE/CVF Conference on Computer Vision and Pattern Recognition Workshops*, 14-19 June, 2020. Doi: 10.1109/CVPRW50498.2020.00341

[8] C. Yang, L. Ding, Y. Chen, and H. Li, "Defending against gan-based deepfake attacks via transformation-aware adversarial faces," In *2021 International Joint Conference on Neural Networks* (IJCNN) IEEE, pp. 1-8, July 2021.

[9] A. Siarohin, S. Lathuilière, S. Tulyakov, E. Ricci, and N. Sebe, "First order motion model for image animation," *Advances in Neural Information Processing Systems* 32, 2019.

[10] M.T. Jafar, M. Ababneh, M. Al-Zoube, and A. Elhassan, "Forensics and analysis of deepfake videos," In *2020 11th international conference on information and communication systems* (ICICS) IEEE, pp. 053-058, April 2020.

[11] A. Siarohin, S. Lathuilière, S. Tulyakov, E. Ricci, and N. Sebe. "Animating arbitrary objects via deep motion transfer," In *CVPR*, pp. 2377-2386, 2019.

[12] D. Afchar, V. Nozick, J. Yamagishi, and I. Echizen, "Mesonet: A compact facial video forgery detection network," *10th IEEE International Workshop on Information Forensics and Security*, (WIFS) 2018. https://doi.org/10.1109/WIFS.2018.8630761

[13] Google Colab, https://colab.research.google.com/

[14] Python, https://www.python.org/

 ISBN 978-86-7466-930-3

Kvarcni kristalni filtar frekvencije 35.4 MHz zasnovan na trećem overtonu

Dragi Dujković, Ana Gavrovska, Lenkica Grubišić, Snežana Dedić-Nešić, Irini Reljin, Ivan Popović

***Apstrakt*— Za savremene telekomunikacije, posebno digitalne, veoma je važno koristiti kvalitetne komponente za prijem, predaju i prenos signala. Među najbitnijim komponentama u takvim sistemima su kristalni filtri, koji su i često korišćene komponente. U ovom radu je opisan kristalni filtar 35,4 MHz zasnovan na kristalnoj jedinki trećeg overtona, kao i korišćene tehničke karakteristike.**

***Ključne reči*—Kristali, filtri, projektovanje, overton, tehničke karakteristike.**

I. Uvod

Potrebno je imati u vidu da mogućnost projektovanja i realizacije kristalnih filtara prema konkretnom zahtevu korisnika pruža pogodnosti u ispunjenju različitih zahteva u pogledu centralne frekvencije filtra, širine propusnog opsega i selektivnosti, toka amplitudske i fazne karakteristike u propusnom opsegu. Mogući su i mnogi specifični zahtevi vezani za klimomehaničke karakteristike, intermodulaciju i druge karakteristike koje diktira primena filtra u specifičnim uslovima. Mali je broj proizvođača koji pružaju mogućnost realizacije kristalnih filtara na osnovu konkretnih zahteva korisnika. Uglavnom se proizvodnja zasniva na realizaciji kataloških tipova filtara [1-7].

U ovom je radu realizovan novi tip kristalnog filtra na frekvenciji 35.4 MHz. Projektovan je filtar koji obezbeđuje ispunjenje postavljenih zahteva. Proračunom filtra definisani su elementi ekvivalentne električne mreže i zahtevi za kristalne jedinke. Ovde zahtevi za kristalne jedinke obuhvataju: dozvoljeni nivo neželjenih rezonancija; frekvencije kristalnih jedinki; dozvoljeno odstupanje frekvencije kristala na sobnoj temperaturi i u radnom temperaturnom opsegu; vrednosti parametara kristalne jedinke; serijsku i paralelnu kapacitivnost; faktor dobrote kristala.

Postupak proizvodnje primenjen u realizaciji ovih filtara može da se uvede u proces proizvodnje svih tipova kristalnih filtara koji imaju slične zahteve u pogledu strogo definisanih električnih karakteristika.

Mogu se razmatrati sledeći iazazovi: ostvarivanje što većeg slabljenja u nepropusnom opsegu filtra i što manjeg slabljenja u propusnom opsegu filtra. Zajedno sa navedenim razmatranjem odvijao se razvoj kristalnih jedinki koje imaju ostvarene sve parametare koje je odredilo projekatvanje filtra. Posebno je vođeno računa o uslovu da se ostvari što veći *Q*-faktor i što veći faktor potiskivanja neželjenih rezonancija.

Q faktor je bezdimenzioni parametar koji opisuje koliko je oscilator ili rezonator nedovoljno prigušen. Približno se definše kao odnos početne energije rezonatora i energije izgubljene u jednom krugu ciklusa oscilovanja. Faktor potiskivanja neželjenih rezonancija je logaritam odnosa amplituda neželjenih signala i signala na centralnoj frekvenciji rezonatora.

Uporedo sa tim je urađena i analiza svih komponenata koji se ugrađuju u filtar i proveren njihov uticaj na osetljivost filtra u pogledu funkcionisanja u radnom temperaturnom opsegu i pri zadatim uslovima rada [10-11].

Rad je organizovan na sledeći način. U drugoj glavi dat je kratak osvrt na potrebe za realizacijom ovakvih filtara. Treća glava je posvećena samom projektovanju filtara. Kristalne jedinke su opisane, kao i njihova realizacija u glavi četiri. Na kraju, u petoj glavi nalazi se zaključak.

II. Realizacija filtara traženih karakteristika

Zahtevane električne karakteristike filtara su direktno povezane sa namenom samog uređaja, a to određuje oblik amplitudske i fazne karakteristike u propusnom opsegu, centralnu frekvenciju filtra, širinu propusnog opsega i selektivnost.

Pored osnovnih karakteristika postoje i karakteristike koje u zavisnosti od toga u kakvim uslovima rada uređaj funkcioniše imaju zahteve koji se odnose na vibracije, udare, potrese, temperaturu, pritisak, vlagu. To su tzv. klimomehanički uslovi rada, ali postoji i dosta drugih specifičnih zahteva.

Ovi kristalni filtri, koji se prema traženoj specifikaciji ne mogu pronaći u katalozima proizvođača, zahtevaju kompletan razvoj uz odgovarajući projekat filtra prema postavljenim zahtevima.

Važna je potreba da se mogu realizovati kristalni filtri na osnovu specifičnih zahteva korisnika. To zahteva razvoj novih tehnoloških postupaka pri proizvodnji, kao i projektovanje filtara i njihovih komponenata. Zbog toga se većina proizvođača bavi proizvodnjom kataloških tipova filtara sa standardnim karakteristikama i komponentama [4–12].

Dragi Dujković – Univerzitet u Beogradu - Elektrotehnički fakultet, , Bulevar Kralja Aleksandra 73, 11120 Beograd, Srbija (e-mail: dragi@etf.bg.ac.rs).

Ana Gavrovska – Univerzitet u Beogradu - Elektrotehnički fakultet, , Bulevar Kralja Aleksandra 73, 11120 Beograd, Srbija (e-mail: anaga777@etf.bg.ac.rs).

Lenkica Grubišić – Institut Mihajlo Pupin, Volgina 15, 11060 Beograd, Srbija (e-mail: lenka@piezo.imp.bg.ac.rs).

Snežana Dedić-Nešić– Institut Mihajlo Pupin, Volgina 15, 11060 Beograd, Srbija (e-mail: snezanadn@gmail.com).

Irini Reljin – Univerzitet u Beogradu -Elektrotehnički fakultet, Bulevar Kralja Aleksandra 73, 11120 Beograd, Srbija (e-mail: irinitms@etf.bg.ac.rs).

Ivan Popović – Univerzitet u Beogradu -Elektrotehnički fakultet, Bulevar Kralja Aleksandra 73, 11120 Beograd, Srbija (e-mail: poppovici@etf.bg.ac.rs).

 ISBN 978-86-7466-930-3

III. PROJEKTOVANJE FILTARA

Na osnovu liste tehničkih zahteva koja je prikazana u tabeli I, završen je projekat željenog filtra. Takođe, na osnovu zahteva u pogledu oblika amplitudske karakteristike u propusnom i nepropusnom opsegu određuje se red filtra i sama mreža koja ispunjava postavljene zahteve. Na slici 1 prikazana je šema jednog filtra. Prilikom proračuna parametara i projektovanja filtra mora se voditi računa i o tolerancijama komponenata koje se ugrađuju u filtar kako bi bile ispunjene tražene karakteristike.

Na osnovu predviđenih gubitaka u mreži, završen je proračun filtra, određena je električna šema i definisani su zahtevi vezani za kristalne jedinke. Projektovanjem filtra moraju se tačno definisati svi parametri kristalnih jedinki, njihove vrednosti i tolerancije. Proračunavaju se i parametri kao što su frekvencija kristala, serijske i paralelne kapacitivnosti kristala i podešenosti frekvencije na sobnoj temperaturi. Takođe se definišu i maksimalna dozvoljena odstupanja frekvencija kristala u radnom temperaturnom opsegu filtra.

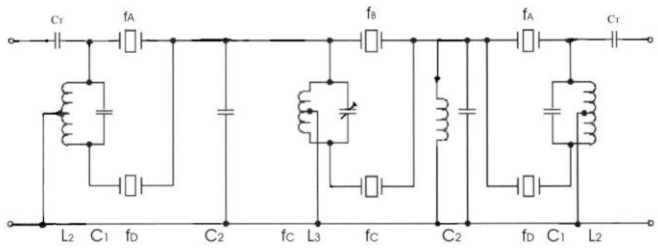

Sl. 1. Električna šema kristalnog filtra.

Prema datim zahtevima urađen je projekat filtra 6-og reda uz Chebyshev aproksimaciju. Razvijene su kristalne jedinke AT-reza sa malim odstupanjem frekvencije (lista tehničkih podataka tačka 8) u širokom temperaturnom opsegu koje ispunjavaju zadate zahteve u vidu položaja i potisnutosti sporednih rezonancija.

Potrebno je napomenuti i da se projektovanjem filtra oodređuju i vrednosti parametara ostalih elemenata, kao što su otpornici, kalemovi i kondenzatori, a takođe i njihov raspored na štampanoj ploči.

Mora se uzeti u obzir da filtri rade na visokim frekvencijama, gde prisustvo parazitnih kapacitivnosti značajno utiče na karakteristike filtara, tako da je raspored elemenata od izuzetnog značaja u podešavanu vrednosti selektivnosti i slabljenja u nepropusnom opsegu filtra [1-5].

IV. PRISTUP ZASNOVAN NA KRISTALNIM JEDINKAMA I REALIZOVANI KRISTALNI FILTAR

Projektovani filtar ima relativno slabljenje u propusnom opsegu od ±4.25 kHz koje je manje od 3dB. Izvan frekvencijskog opsega od ±20 kHz slabljenje je veće od 60 dB . U širem opsegu frekvencija, do ±5 MHz, relativno slabljenje je veće od 60 dB.

Minimalno pogonsko slabljenje filtra je manje od 6 dB. Ulazna i izlazna otpornost filtra iznose 50 Ω. Radni temperaturni opseg filtra je -10º C do +60 ºC. Temperaturni opseg skladištenja, odnosno opseg temperatura u kojima filtar neće promeniti karakteristike dok se čuva u skladištu je -40 ºC do +85 ºC.

Filtar je smešten u kućište dimenzija (38,4×18.2×15.9) mm. Detalji svih tehničkih karakteristika filtra su dati u Tabeli I.

Nizom eksperimenata ustanovljen je povećan škart usled lomova na mašinama za glačanje i poliranje pri obradi pločica čiji je odnos prečnika i debljine Φ/t>100. S obzirom da kvarcna pločica prečnika Φ=5 mm, frekvencije 35.4 MHz osnovne učestanosti, ima odnos prečnika i debljine Φ/t=106.38 pristupilo se realizaciji kristala trećeg overtona čiji je Φ/t=35.46 čime je, sa druge strane zadovoljen uslov za planparalelni (PP) oblik pločica trećeg overtona (Φ/t>35).

Overton je pojava odziva na rezonatoru koja je na frekvenciji 3, 5 ili 7 puta većoj od osnovne frekvencije rezonatora. Ova pojava se koristi da bi se postigle veće frekvencije rada kristalnog rezonatora.

U projektu mikrominijaturnih kristalnih jedinki trećeg overtona učestanosti 35.4MHz vodilo se računa o prečniku elektrode d=1.63mm i debljini nanetog filma t = 2,9x10-7m zbog zahteva za položaj i potisnutost sporednih rezonancija. S obzirom da se radi o tankim filmovima kao elektrodni materijal korišćen je aluminijum. Podešavanje frekvencije je hemijsko u sodi i anodnom oksidacijom. Sve kristalne jedinke su posle grupnog naparavanja i cementiranja stajale na vazduhu 24h radi formiranja stabilnog prirodnog oksidnog sloja. Kvarcne pločice su planparalelne (PP) prečnika Φ=5 mm i realizovane su od kvarca faktora dobrote Q>1.8 x10^6 bez strukturnih defekata i grešaka pakovanja. Kristalne jedinke montirane su u držač tipa RW-HC45.

Realizovane kristalne jedinke AT-reza zadovoljavaju zahteve za položaj i potisnutost sporednih rezonancija i dozvoljeno odstupanje frekvencije u radnom temperaturnom opsegu.

Na slici 2 prikazan je realizovani filtar. Filtar je smešten u standardno kućište koje je prikazano na slici 3.

Sl. 2. Realizovani kristalni filtar.

 ISBN 978-86-7466-930-3

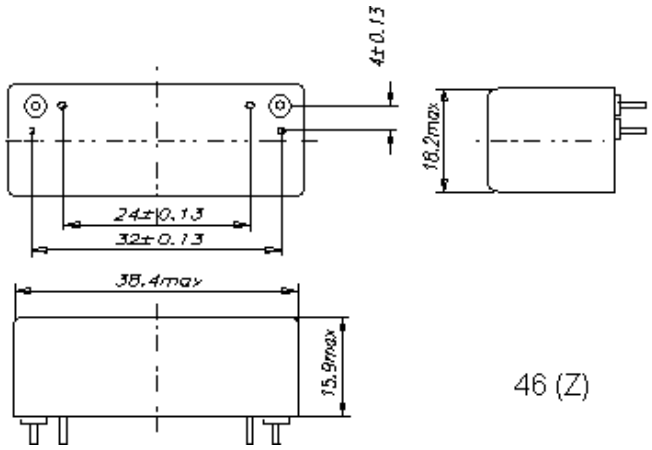

Sl. 3. Kućište filtra.

Ispitivanje filtara koje je izvršeno na sobnoj temperaturi i u radnom temperaturnom opsegu od -10˚C do +60˚C urađeno je na analizatoru spektra HP 8568A. Merenjima je utvrđeno da filtar zadovoljava tražene električne karakteristike.

Rezultati merenja amplitudske karakteristike filtra na sobnoj temperaturi prikazani su u dijagramima na slici 4.

Lista tehničkih podataka za kristalne jedinke za filtre 35,4 MHz je sledeća:

1.	Kućište	RW-HC45
2.		
3.	frekvencija	f_1 = 35392.53 kHz f_2 = 35401.27 kHz f_1 = 35393.73 kHz f_2 = 35400.07 kHz
4.	*Q*-faktor	> 120000
5.	dinamička kapacitivnost	C_1 = 380 apF ± 10%
6.	paralelna kapacitivnost	C_o = 1 pF ± 5%
7.	dinamička otpornost	R_1 < 90 Ω
8.	podešenost	*df/f*=±5 ppm
9.	odstupanje	*df/f*=±15 ppm
10.	starenje	*df/f*=1 ppm/god
11.	radni temperaturni opseg	-10÷+90˚C
12.	neželjene rezonancije	A. f_0+70 kHz–bez f_n

TABELA I

TEHNIČKE KARAKTERISTIKE FILTARA

Karakteristike	***Vrednosti***
Centralna frekvencija(CF)	35,4 MHz
Širina propusnog opsega na 2 dB	± 3 kHz
Širina propusnog opsega na 3 dB	± 4.25 kHz
Talasnost u propusnom opsegu	2 dB max u opsegu ± 7.5 kHz
Širina nepropusnog opsega na 60 dB	± 20 kHz max
Relativno slabljenje u nepropusnom opsegu	60 dB min za ± 5 MHz
Minimalno pogonsko slabljenje	6 dB max
Ulazna impedansa	50 Ω
Izlazna impedansa	50 Ω
Radni temperaturni opseg	-10 ºC до +60 ºC
Temperaturni opseg skladištenja	-40 ºC до +85 ºC

V. ZAKLJUČAK

Pored proračuna i realizacije kristalnog filtra, razvijena je i nova kristalna jedinka. Ovakvi kristalni filtri predstavljaju novi proizvod, jer su u njemu korišćene nove tehnologije i nove komponente. Ovi proizvodi imaju širok dijapazon primena i veliku upotrebnu vrednost i ističu se svojom cenom i svojim kvalitetom, tako da se mogu smatrati konkurentnim na tržištu. Navedene karakteristike i konkurentnost na tržištu daju perspektivu razvoju novih elektronskih sklopova i proizvoda zasnovanih na kristalnim jedinkama.

U daljem razvoju ovih i sličnih uređaja treba ići na usvajanje novih tehnologija izrade kristalnih jedinki i upotrebe novih i kvalitetnijih komponenti u kolu elektronskih sklopova novih uređaja.

ZAHVALNICA

Istraživanja opisana u ovom radu su finansirana od strane Ministarstva za obrazovanje, nauku i tehnološki razvoj Republike Srbije. Broj ugovora 451-03-68/2022-14/200103

 ISBN 978-86-7466-930-3

LITERATURA

[1] S. Dedić-Nešić "Prilog projektovanju kristalnih filtara sa linearnom faznom karakteristikom", magistarska teza, Elektrotehnički fakultet, Univezitet u Beogradu, 1991.

[2] R. G. Kinsman, "A history of crystal filters," in Proc. of the 1998 IEEE Int. Frequency Control Symposium, pp. 563-570, 1998.

[3] H. J. Blinchikoff, A. I. Zverev "Filtering in the Time and Frequency Domains" John Wiley and Sons, Inc, 1976.

[4] D. S. Humpherys "The Analysis, Design and Synthesis of Electrical Filters" Prentice Hall, Englewood Clifs, N.J. 1970.

[5] S. Dedić-Nešić, D. Dujković, L. Grubišić, I. Reljin, B. Reljin, "Novi visokokvalitetni 90.1105 MHz filtri za komunikacije u rudnicima," ETRAN, 2010.

[6] D. Dujković, B. Reljin, S. Dedić-Nešić, L. Grubišić, D. Jevtić, "Novi kristalnih filtar F121," ETRAN, 2012.

[7] D. M. Dujković, S. Dedić–Nešić , L. Grubišić, A. Gavrovska, and I. Reljin, "High-quality crystal filter: Design and realization," *Telfor J.*, vol. 5, no. 2, pp. 118–122, 2013.

[8] L. Grubišić, S. Dedić–Nešić, D. M. Dujković, , B. Reljin, "Novi tip kristalne jedinke za filtre namenjene za rad u posebnim klimo mehaničkim uslovima", ETRAN, 2012, EK2.6-1-4, Banja Vrućica 2011.

[9] D. Dujković, S. Dedić Nešić, L. Grubišić, B. Reljin, I. Reljin, "Crystal Filter 50 MHz for Applications in Specific Environmental Conditions," in Proc. 10th Int. Conf. on Telecommunication in Modern Satellite Cable and Broadcasting Services (TELSIKS), 2011, vol. 1. pp. 253-256, Nis, Serbia, 2011.

[10] D. M. Dujković, S. Dedić Nešić, L. Grubišić, M. Paskaš, and Irini Reljin, "New 76.8375 MHz Crystal filter Based on Third overtone Crystal units," 28th Telecommunications forum TELFOR 2020, pp.177-180, 2020.

[11] D. M. Dujković, I. Reljin, L. Grubišić, S. Dedić–Nešić, and A. Gavrovska, "Kristalni filtri za opseg frekvencija 150-170MHz," ETRAN, EK 1-1, pp. 213-216, Stanišići 2021.

[12] D. M. Dujković, S. Dedić–Nešić, L. Grubišić, I. Reljin, and A. Gavrovska, "New stop band 48 MHz crystal filter," Telfor Proceedings, pp. 249-252, Belgrade 2021.

ABSTRACT

In modern telecommunications, especially digital, it is very important to use quality components for receiving, sending and transmitting signals. Among the most valuable components are crystal filters, which are also commonly used components. The paper describes a 35.4 MHz crystal filter based on crystalline units of the third overtone and applied technical characteristics.

Quartz crystal filter 35.4 MHz based on crystalline units of the third overtone

Dragi Dujkovic, Ana Gavrovska, Lenkica Grubisic, Snezana Dedic-Nesic, Irini Reljin

 ISBN 978-86-7466-930-3

FILTER - TEST RECORD

1. nominal centre freq.	fc	:	35.400000 MHz		
2. delta fc		:	-306 Hz		
3. bandwidth	at 2.0 dB	:	10.879 kHz		
	w.r.t. fc	:	-5.745 kHz		+5.133 kHz
4. ripple		:	0.00 dB	in fm +/-	3.000 kHz
5. transducer attenuation		:	2.6 dB		
6. attenuation at fc		:	2.6 dB		
7. stop bandwidth	at	:	60.0 dB		
	at fc	: -	14.498 kHz	+	15.713 kHz
8. ultimate attenuation	>=	:	79.6 dB		
	from	:	30.400000 MHz	to	35.380000 MHz
	>=	:	90.6 dB		
	from	:	35.420000 MHz	to	40.400000 MHz

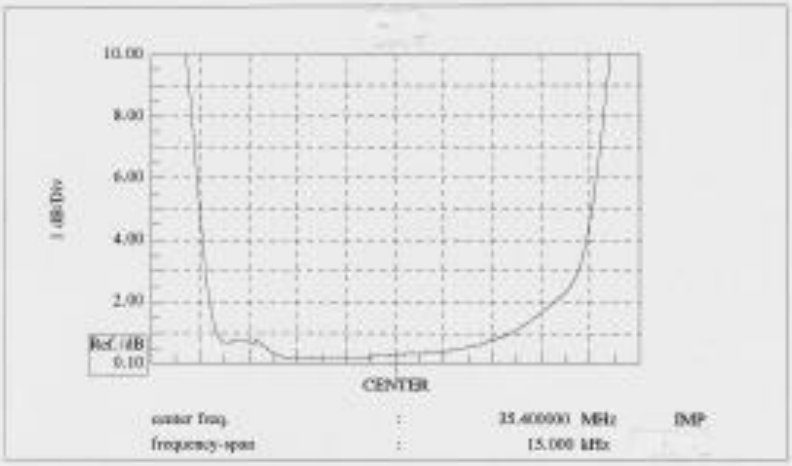

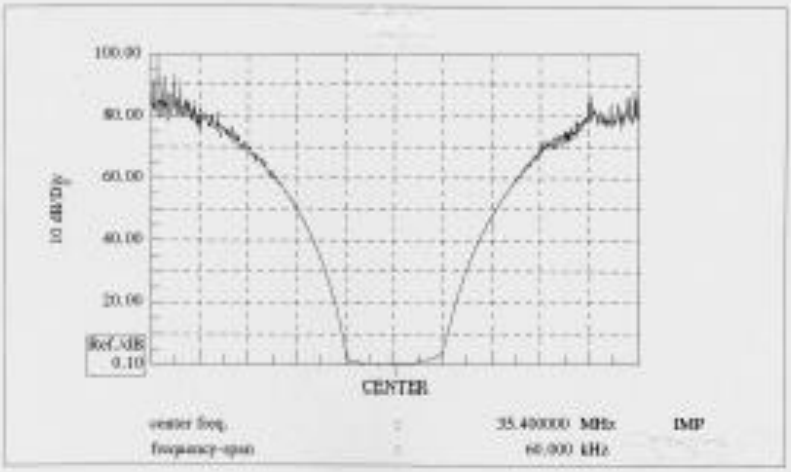

Sl. 4. Rezultati merenja amplitudske karakteristike filtra 35,4 MHz na sobnoj temperaturi.

 ISBN 978-86-7466-930-3

Primena vremensko-frekvencijskih metoda kod analize spektra u kognitivnom radiju

Nenad Stojanović, Milenko Andrić, Dimitrije Bujaković, Boban Bondžulić i Vladimir Ristić

***Apstrakt*—U radu je izvršena analiza primene tri metode vremensko-frekvencijske analize signala za potrebe analize spektra kod kognitivnog radija. Analiza je sprovedena modelovanim i realnim signalima za aditivni beli Gausov šum različitog odnosa signal/šum. Performanse metoda su analizirane kroz promene odnosa signal/šum i praga detekcije, određivanjem verovatnoće lažnog alarma, verovatnoće propuštene detekcije i verovatnoće ispravne detekcije. Pokazano je da se metode vremensko-frekvencijske analize signala mogu efikasno koristiti za potrebe analize spektra uz odgovarajuću optimizaciju parametara.**

***Ključne reči*—Frekvencijsko skakanje, kognitivni radio, vremensko-frekvencijska analiza spektra.**

I. Uvod

EKSPONENCIJALNI rast broja bežičnih uređaja i sistema prenosa, kao i zahtevi korisnika za većim brzinama prenosa i boljem kvalitetu usluge, uticali su na sve izraženije probleme kod dodele spektra i uopšte pristupu radio spektru. Jedno od rešenja predstavlja kognitivna radio tehnologija, čiji je cilj da poveća spektralnu efikasnost koristeći delove sprektra koje ne koristi primarni korisnik za prenos signala sekundarnih korisnika [1]. Sekundarni korisnici određenog spektralnog opsega ni u kom slučaju ne smeju ometati primarne korisnike. U tom cilju, ovako koncipiran pristup radio spektru, odnosno upravljanju spektrom (eng. *Spectrum Management*) se sastoji iz četiri koraka [2]:

- analiza spektra (eng. *Spectrum Sensing*),
- donošenje odluka (eng. *Spectrum Decision*),
- deljenje spektra (eng. *Spectrum Sharing*) i
- mobilnost spektra (eng. *Spectrum Mobility*).

Kognitivni radio se može definisati kao unapređeni softverski definisani radio, sa ostvarenom sposobnosti učenja i zaključivanja, odnosno kognitivnost [3]. Jednu od definicija dao je i američki FCC (*Federal Communication Commision*) po kojem kognitivni radio predstavlja bežični uređaj koji dinamički detektuje neiskorišćene delove spektra i koristi ih tako da ni na koji način ne ometa primarne korisnike u tom opsegu [4].

Najvažnija funkcija kognitivnog radija je analiza spektra, pri čemu je osnovni izazov analize spektra detekcija signala male snage sa malom verovatnoćom propuštene detekcije u uslovima niskog odnosa signal/šum (eng. *Signal to Noise Ratio*, SNR). Postoji više različitih klasifikacija tehnika za analizu spektra [5, 6, 7]. Jedna od najčešće korišćenih je podela na: tehnike analize spektra za detekciju primarnih predajnika, tehnike analize spektra za detekciju primarnih prijemnika i tehnike analize spektra zasnovane na temperaturi interferencije.

Vremensko-frekvencijske metode analize signala se koriste za analizu spektra kognitivnog radija [8]. U [9] je izvršena analiza spektra kada je primarni signal digitalna televizija, odnosno OFDM (*Orthogonal Frequency Division Multiplexing*) signal. Autori u [10] predlažu modifikaciju vremensko-frekvencijskih metoda za analizu spektra u prisustvu OFDM signala. U [11] su autori pored OFDM signala, razmatrali i signal sa frekvencijskim skakanjem. Analiza spektra radio sistema TETRA (*Terrestial Trunked Radio*) je predložena u [12]. Karakteristika svih navedenih radova je korišćenje modelovanih signala za analizu spektra kognitivnog radija.

Slična analiza spektra vrši se tokom elektronskog rata u cilju prikupljanja informacija, ali bez potrebe za iskorišćenjem spektralnih šupljina. Kod ovakvih sistema neke od osnovnih funkcija su detekcija izvora zračenja, klasifikacija i identifikacija emitera, određivanje lokacije emitera i njegovo praćenje. Sve ove funkcije potrebno je obavljati u veoma kompleksnom okruženju u realnom vremenu.

U ovom radu su analizirane metode vremensko-frekvencijske analize signala za potrebe analize spektra kognitivnog radija. Razmatran je signal sa frekvencijskim skakanjem koji se često koristi u vojnim radio sistemima. Frekvencijsko skakanje predstavlja tehniku prenosa koja se zasniva na skokovitoj promeni frekvencije nosioca u širem opsegu nego što je to neophodno [13]. Za potrebe analize razvijen je simulacioni model, a takođe su korišćeni i snimljeni realni signali iz baze signala [14].

Ostatak rada je organizovan na sledeći način. U drugom delu rada ukratko su opisane korišćene metode za vremensko-frekvencijsku analizu signala. U trećem delu rada opisana je

Nenad Stojanović – Vojna akademija, Univerzitet odbrane u Beogradu, Veljka Lukića Kurjaka 33, 11000 Beograd, Srbija (e-mail: nivzvk@hotmail.com).

Milenko Andrić – Vojna akademija, Univerzitet odbrane u Beogradu, Veljka Lukića Kurjaka 33, 11000 Beograd, Srbija (e-mail: andricsmilenko@gmail.com).

Dimitrije Bujaković – Vojna akademija, Univerzitet odbrane u Beogradu, Veljka Lukića Kurjaka 33, 11000 Beograd, Srbija (e-mail: dimitrijebujakovic@gmail.com).

Boban Bondžulić – Vojna akademija, Univerzitet odbrane u Beogradu, Veljka Lukića Kurjaka 33, 11000 Beograd, Srbija (e-mail: bondzulici@yahoo.com).

Vladimir Ristić – Vojna akademija, Univerzitet odbrane u Beogradu, Veljka Lukića Kurjaka 33, 11000 Beograd, Srbija (e-mail: vladarist@gmail.com).

 ISBN 978-86-7466-930-3

metodologija analize spektra. Analiza modelovanih signala sa frekvencijskim skakanjem je data u četvrtom poglavlju, dok je u petom izvršena analiza realnih, akviziranih signala sa frekvencijskim skakanjem. U poslednjem odeljku dati su najvažniji zaključci i budući pravci istraživanja.

II. METODE VREMENSKO-FREKVENCIJSKE ANALIZE SIGNALA

Najčešće korišćena vremensko-frekvencijska predstava signala je spektrogram. Spektrogram predstavlja energetsku verziju vremenski zavisne Furijeove transformacije (eng. *Short-time Fourier Transform*, STFT). STFT je definisana kao [15]:

$$STFT(n,k)=\sum_{m=-N/2}^{N/2} w(m)x(n+m)e^{-j(2\pi/N)mk}, \quad (1)$$

gde su $x(n+m)$ signal koji se analizira, $w(m)$ prozorska funkcija, dok je broj tačaka za izračunavanje Furijeove transformacije $N+1$. Spektrogram je definisan kao:

$$SPEC(n,k)=\left|STFT(n,k)\right|^2. \quad (2)$$

Vremenska i frekvencijska rezolucija određene su dužinom prozorske funkcije. Smanjenjem dužine prozora dobija se bolja vremenska rezolucija čime se negativno utiče na frekvencijsku rezoluciju. Povećanjem dužine prozora, smanjuje se vremenska rezolucija, ali se poboljšava predstava signala u frekvencijskom domenu. Prozori se međusobno mogu preklapati ili ne. Povećanjem preklapanja prozora poboljšava se vremenska rezolucija [16].

Vignerova vremensko-frekvencijska distribucija (eng. *Wigner Distribution*) je razvijena kao optimalna za predstavu jednokomponentnih linearno frekvencijski modulisanih signala u vremensko-frekvencijskom domenu. Pri analizi višekomponentnih signala, pojavljuju se komponente koje se ne nalaze u originalnom signalu, što predstavlja jedan od nedostataka ove transformacije. Kompleksnost izračunavanja ove distribucije je veoma velika, što je još jedan nedostatak. Pseudo Vigner-Vilova vremensko-frekvencijska distribucija signala (eng. *Pseudo Wigner-Ville Distribution*, PWV) predstavlja Vignerovu raspodelu analitičkog signala i može se predstaviti primenom STFT kao [17]:

$$\begin{aligned} WD(n,k)&=\sum_{i=-N/2}^{N/2} STFT(n,k+i)STFT^*(n,k-i)= \\ &=\left|STFT(n,k)\right|^2+2\,\mathrm{Re}\left\{\sum_{i=1}^{N/2} STFT(n,k+i)STFT^*(n,k-i)\right\} \end{aligned}, \quad (3)$$

gde je sa * označena konjugovano kompleksna vrednost. Poređenjem (2) i (3) uočava se da kod Vignerove raspodele postoji dodatni član koji povećava broj računskih operacija i time povećava složenost ovog algoritma u odnosu na spektrogram.

U cilju postizanja kompromisa između Vignerove raspodele i spektrograma, uz iskorišćenje prednosti koje daje Vignerova raspodela u smislu predstave signala i smanjenja računarske složenosti što je karakteristika spektrograma, predložen je S-metod, koji se definiše kao [18]:

$$SM_L(n,k)=\sum_{i=-L}^{L} STFT(n,k+i)STFT^*(n,k-i), \quad (4)$$

gde je L frekvencijska dužina prozora. Za slučaj kada je $L=0$, S-metod predstavlja spektrogram, dok je za slučaj kada je $L=N/2$, S-metod zapravo pseudo Vignerova raspodela [17].

III. ANALIZA SPEKTRA KORIŠĆENJEM VREMENSKO-FREKVENCIJSKIH METODA

U ovom istraživanju predložena je analiza spektra kognitivnog radija. Analiza spektra izvršena je na osnovu dve hipoteze:

$$\begin{aligned} H_0&: y[n]=z[n], n=1,...,N \\ H_1&: y[n]=x[n]+z[n], n=1,...,N \end{aligned}, \quad (5)$$

gde je $y[n]$ signal čiji se spektar analizira, $x[n]$ je signal primarnog korisnika, dok je $z[n]$ aditivni beli Gausov šum. Hipoteza H_0 je tačna kada u analiziranom spektru nema prisustva signala primarnog korisnika, dok je hipoteza H_1 tačna kada postoji primarni signal.

Analiza spektra se sprovodi kroz sledeće korake:

1. realizacija vremensko-frekvencijske analize spektra korišćenjem neke od opisanih metoda (spektrogram, S-metod za $L=2$ i pseudo Vigner-Vilova raspodela),
2. poređenje amplituda spektralnih komponenti sa pragom detekcije u svakom vremenskom binu i
3. donošenje odluke da li postoji primarni signal u određenom vremenskom intervalu i ako postoji koji deo spektra zauzima.

Analiza efikasnosti rada kognitivnog radija realizovana je kroz verovatnoće ispravne detekcije (P_d), lažnog alarma (P_{fa}) i propuštene detekcije (P_{miss}). Određivanje da li je signal primarnog korisnika ispravno detektovan vršeno je po vremenskim binovima, koji su određeni brojem odbiraka korišćenim za izračunavanje spektra nekom od opisanih vremensko-frekvencijskih metoda. Analiza je sprovedena za slučaj kada se u radio spektru javlja emisija samo jednog primarnog korisnika.

Određivanje definisanih verovatnoća vršena je po vremenskim binovima prema sledećem:

- ukoliko je detektovan signal u frekvencijskom opsegu u kojem je i emitovan, izvršena je uspešna detekcija,
- ukoliko nije detektovan signal kada nije ni bilo emisije, izvršena je uspešna detekcija,
- ukoliko je detektovan signal u nekom frekvencijskom opsegu u kome primarni korisnik nije vršio emisiju, došlo je do pojave lažnog alarma,
- ukoliko primarni signal nije detektovan u opsegu u kome je postajala emisija došlo je do propuštene detekcije,

 ISBN 978-86-7466-930-3

– ukoliko je detektovano više signala, od kojih je jedan signal primarnog korisnika, izvršena je uspešna detekcija,
– ukoliko je detektovano više signala, ali nijedan od njih nije u opsegu gde je emitovan primarni signal, došlo je do propuštene detekcije,
– ukoliko je detektovano više signala, a primarni korisnik nije vršio emisiju, došlo je do pojave lažnog alarma,

Testiranja su vršena Monte-Karlo simulacijama, pri čemu je zbog slučajnog procesa u kanalu izazvanog aditivnim belim Gausovim šumom, postupak ponavljan 100 puta, nakon čega je vršeno usrednjavanje rezultata. Izabran broj ponavljanja testova je u skladu sa [11]. Analizirani su spektri modelovanog signala i spektri realnog signala sa sporim frekvencijskim skakanjem primenom spektrograma, S-metoda za L=2 i pseudo Vigner-Vilove distribucije.

IV. Analiza spektra modelovanog signala

Za potrebe analize razvijen je simulacioni model radio sistema prenosa sa frekvencijskim skakanjem koji predstavlja signal primarnog korisnika. Modelovani sistem koristi opseg od 30-80 MHz sa sporim frekvencijskim skakanjem, tako da se tokom jednog skoka prenosi 50 informacionih simbola. Korišćen je BFSK (*Binary Frequency Shift Keying*) modulacioni postupak. Generisani signal je trajanja nešto više od dve sekunde. Snaga aditivnog belog Gausovog šuma menjana je promenom njegove varijanse.

Na Sl. 1 prikazane su verovatnoće lažnog alarma i propuštene detekcije u odnosu na SNR za tri analizirane metode vremensko-frekvencijske analize signala (spektrogram, S-metod za L=2 i pseudo Vigner-Vilova distribucija). Tokom analize, korišćeno je 128 odbiraka (N=128) za potrebe analize spektra sa preklapanjem 50%. Hamingov (*Hamming*) prozor je korišćen. Prag detekcije je postavljen na 50% maksimalne vrednosti snage simuliranog signala primarnog korisnika.

Analizom Sl. 1 se može uočiti da za pozitivne vrednosti SNR gotovo da nema slučajeva propuštene detekcije i lažnog alarma. Smanjenjem SNR, dolazi do porasta verovatnoća lažnog alarma i propuštene detekcije u intervalu od -10 do 0 dB. Kod verovatnoća propuštene detekcije, spektrogram i S-metod imaju rast, a nakon toga, za još niže vrednosti SNR, ponovo pad i vraćanje na vrednosti približno jednake nuli. Kod PWV takođe postoji ovaj rast verovatnoće propuštene detekcije, ali je on zanemarljiv u odnosu na vrednosti dobijene korišćenjem druge dve metode. Pad ovih vrednosti se javlja zbog povećane snage šuma pa je detekcija signala češća, te stoga raste verovatnoća ispravne detekcije. Korišćenjem spektrograma i S-metoda, verovatnoće lažnog alarma za vrednosti SNR niže od -10 dB daju konstantnu vrednost, od oko 0.2. Verovatnoća lažnog alarma kod PWV raste postepeno dok ne dostigne vrednost približno jedinici. Kod PWV, zbog velike rezolucije detektovan je veliki broj spektralnih komponenti šuma, kao i međukomponenti signala primarnog korisnika, pa je verovatnoća lažnog alarma veća nego što je to slučaj kod druge dve metode.

Kako je u otežanim uslovima rada teško svesti verovatnoće lažnog alarma i propuštene detekcije na nulu, sa stanovišta realizacije kognitivnog radija povoljnije je obezbediti veću verovatnoću lažnog alarma u odnosu na verovatnoću propuštene detekcije. Smanjivanjem verovatnoće propuštene detekcije mogućnost ometanja primarnog korisnika svodi se na minimum.

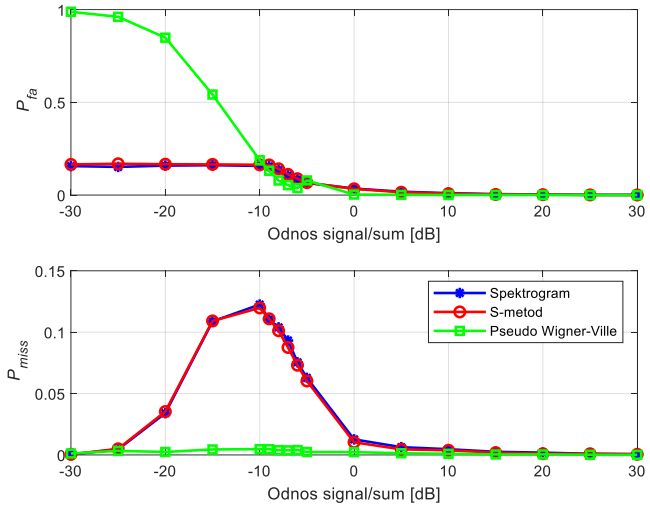

Sl. 1. Verovatnoća lažnog alarma i verovatnoća propuštene detekcije u zavisnosti od odnosa signal/šum kod simuliranog primarnog signala.

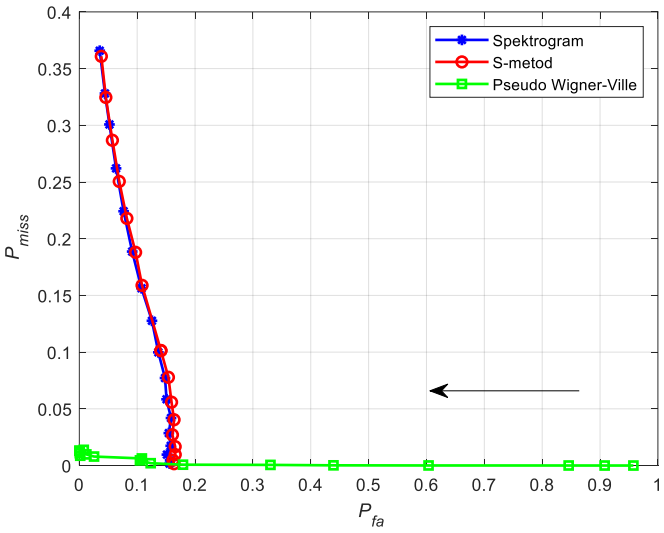

Sl. 2. Odnos verovatnoće propuštene detekcije i verovatnoće lažnog alarma za različite vrednosti praga detekcije kod simuliranog primarnog signala.

Na Sl. 2 prikazan je odnos verovatnoće propuštene detekcije u odnosu na verovatnoću lažnog alarma za sve tri analizirane metode vremensko-frekvencijske analize signala. Krive na Sl. 2 dobijene su za konstantnu vrednost SNR od -8 dB i dužinu prozora od 128 odbiraka, sa preklapanjem 50%. Promenom praga detekcije od 10% do 90% maksimalne vrednosti snage primarnog signala menjaju se odnosi verovatnoće lažnog alarma i verovatnoće propuštene detekcije. Vrednost SNR od -8 dB je uzeta jer se u tom

 ISBN 978-86-7466-930-3

intervalu vrednosti SNR narušava primarni signal dovoljno da se može testirati efikasnost metoda pri radu u otežanim uslovima. Za niske vrednosti praga detekcije, povećava se verovatnoća lažnog alarma, a smanjuje verovatnoća propuštene detekcije i obrnuto. Spektrogram i S-metod su pokazali približno slične rezultate, dok je primenom PWV ostvarena mala verovatnoća propuštene detekcije za različite vrednosti praga detekcije. Ipak, iako PWV ima malo propuštenih detekcija, veliki broj detekcija lažnog alarma onemogućava korišćenje spektra od strane sekundarnih korisnika. Strelica na slici pokazuje smer povećanja praga detekcije.

V. Analiza spektra realnog signala

Testiranje mogućnosti primene vremensko-frekvencijskih metoda analize signala u kognitivnom radiju izvršeno je na realnim signalima iz dostupne baze prikupljenih telekomunikacionih signala [14]. Navedena baza je, prema saznanjima autora, jedina dostupna baza telekomunikacionih signala u razmatranom opsegu učestanosti, a da je pogodna za vremensko-frekvencijsku analizu signala, s obzirom da je primarna namena korišćene baze klasifikacija različitih modulacionih postupaka i tehnika prenosa. Signali su prikupljani pomoću analizatora spektra koji je bio kablom direktno povezan sa radio uređajem kao generatorom signala, čime je pojava šuma prilikom snimanja signala bila smanjena u najvećoj mogućoj meri. U bazi signala postoji nekoliko različitih tipova modulisanih signala, a za potrebe analize u ovom radu korišćeni su samo signali sa frekvencijskim skakanjem. Snimljeni signali su trajanja nešto dužeg od dve sekunde. Radio uređaj je podešen tako da koristi opseg od 30 do 80 MHz za potrebe prenosa frekvencijskim skakanjem. Uređaj koristi 8-CPFSK (*Continuous Phase FSK*) modulaciju. U skladu sa brzinom promene frekvencije nosioca, uređaj podržava samo sporo frekvencijsko skakanje.

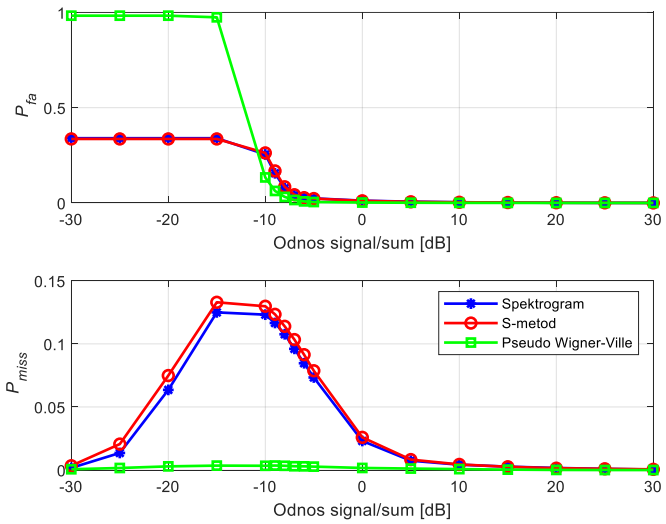

Sl. 3. Verovatnoća lažnog alarma i verovatnoća propuštene detekcije u zavisnosti od odnosa signal/šum kod realnog primarnog signala.

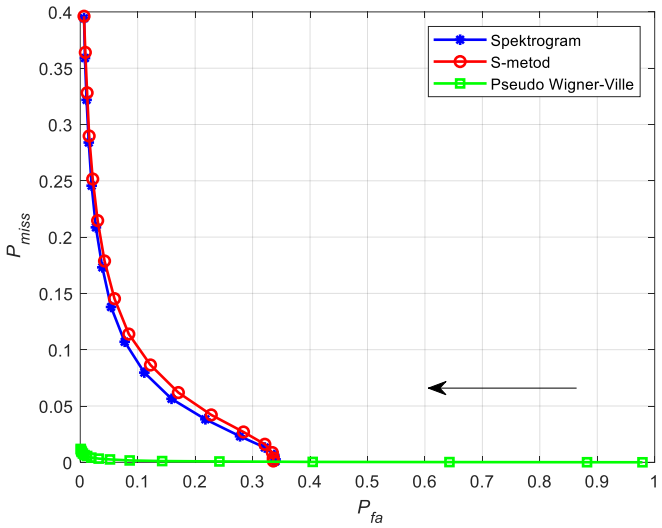

Sl. 4. Odnos verovatnoće propuštene detekcije i verovatnoće lažnog alarma za različite vrednosti praga detekcije kod realnog primarnog signala.

Na Sl. 3 su prikazane verovatnoće lažnog alarma i propuštene detekcije u zavisnosti od SNR, gde su korišćeni isti parametri za vremensko-frekvencijske metode kao i kod modelovanih signala. Dobijeni rezultati su veoma slični u odnosu na slučaj analize modelovanih signala prikazanih na Sl. 1. Dobijene vrednosti za verovatnoću propuštene detekcije su gotovo identične u slučaju modelovanih i realnih signala. Kod verovatnoće pojave lažnog alarma, korišćenjem PWV, za više vrednosti SNR u odnosu na modelovani signal, dostiže se verovatnoća bliska jedinici. Spektrogram i S-metod za niske vrednosti SNR dostižu vrednosti verovatnoće lažnog alarma oko 0.4, što je nešto više nego kod modelovanog signala. Na ovu razliku utiče i šum koji se javio tokom snimanja signala.

Sl. 4 ilustruje odnos verovatnoće propuštene detekcije u odnosu na verovatnoću lažnog alarma, za prozor dužine 128 odbiraka uz 50% preklapanja, SNR=-8 dB i za različite vrednosti praga detekcije u istom opsegu kao i kod modelovanih signala. Dobijene krive su veoma slične kao pri analizi modelovanih signala, uz neznatno više vrednosti verovatnoća lažnog alarma i propuštene detekcije u slučajevima primene spektrograma i S-metoda. Primenom PWV ostvarena je mala verovatnoća propuštene detekcije, čime će se postići neometan rad primarnog korisnika. I na ovoj slici strelica pokazuje smer povećanja praga detekcije.

Na Sl. 5 dat je uporedni prikaz vremensko-frekvencijskih distribucija realnih i simuliranih signala. Slike su prikazane za slučaj kada je SNR=-8 dB, prag detekcije postavljen na 50% amplitude primarnog signala, a broj odbiraka za analizu spektra je 128 uz polovinu odbiraka koji se preklapaju u sledećem intervalu analize. Na slikama je prikazan samo deo vremena signala, u trajanju od oko 100 ms, zbog preglednosti. Sa slika se jasnije uočavaju promene frekvencija nakon određenog vremena korišćenjem spektrograma i S-metode, bilo da su u pitanju modelovani ili realni signali, uprkos niskoj vrednosti SNR. Korišćenjem PWV, uprkos većoj rezoluciji, zbog pojave međuspektralnih komponenti, energija signala je rasuta i ne mogu se uočiti tačne frekvencije signala

 ISBN 978-86-7466-930-3

tokom određenih vremenskih perioda. Iz tog razloga je češća pojava lažnih alarma kod PWV nego kod spektrograma i S-metode. Nešto kvalitetnija rezolucija za isti period prikaza signala dobijen je kod modelovanog signala zbog veće frekvencije odabiranja prilikom generisanja signala u odnosu na frekvenciju odabiranja prilikom snimanja realnih signala. Kod modelovanih signala, uočavaju se dve noseće frekvencije u zavisnosti od poslatog simbola, u toku jednog skoka zbog korišćenja BFSK modulacije.

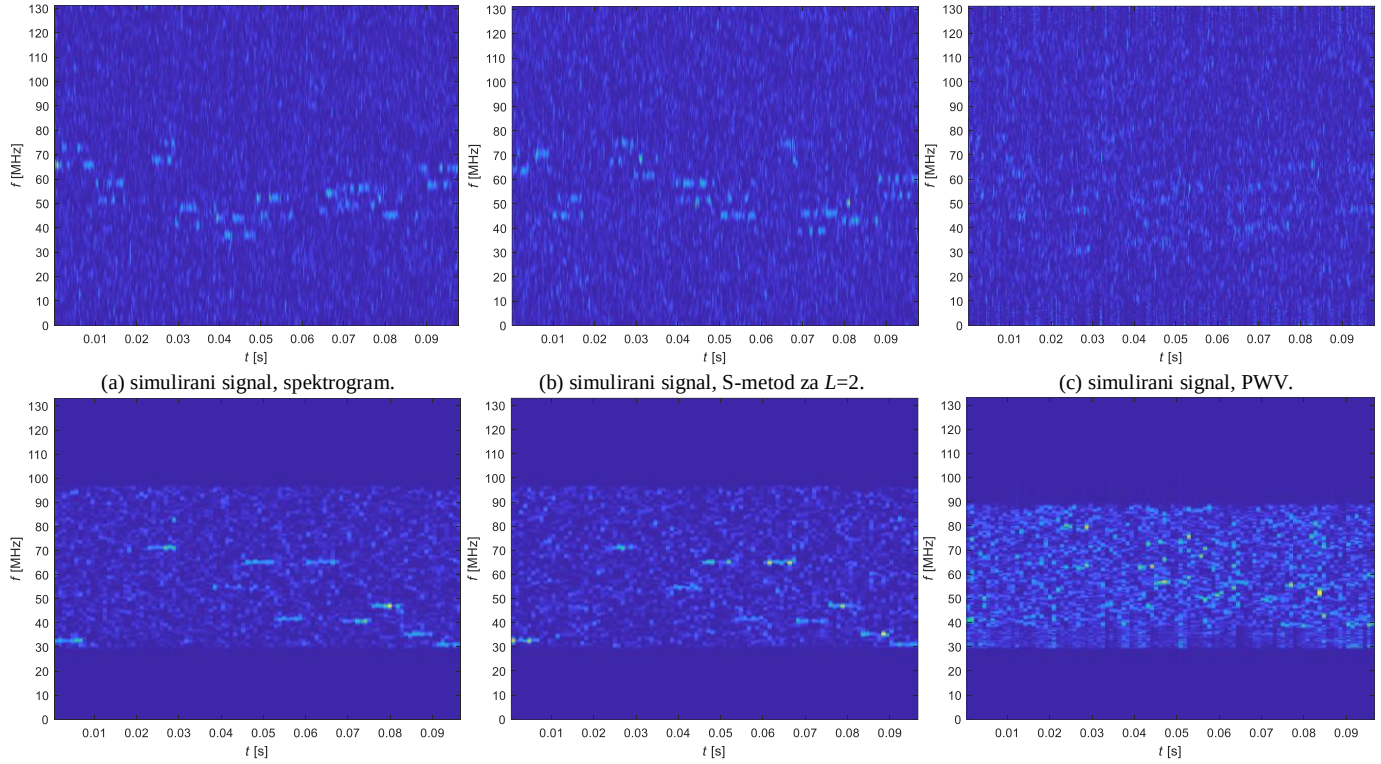

(a) simulirani signal, spektrogram. (b) simulirani signal, S-metod za L=2. (c) simulirani signal, PWV.

(d) realni signal, spektrogram. (e) realni signal, S-metod za L=2. (f) realni signal, PWV.

Sl. 5. Vremensko-frekvencijski prikaz simuliranog i realnog signala za SNR = -8 dB.

VI. Zaključak

U radu je izvršena analiza mogućnosti upotrebe tri metode vremensko-frekvencijske analize signala kognitivnog radija prilikom analize spektra. Za potrebe analize, metode su testirane na modelovanom signalu i snimljenom realnom signalu frekvencijskog skakanja.

Utvrđeno je da dobre performanse za potrebe analize spektra kod kognitivnog radija pokazuje pseudo Vigner-Vil zbog veoma male verovatnoće propuštene detekcije. Ipak, zbog svoje računarske složenosti nije pogodan za implementaciju u sistemima koji za cilj imaju rad u realnom vremenu. Spektrogram je pokazao performanse koje bi bile zadovoljavajuće uz određenu optimizaciju pre svega u broju odbiraka korišćenih za analizu spektra, jer je moguće postići male verovatnoće propuštene detekcije uz male verovatnoće lažnog alarma, čime bi se pored efikasne analize spektra uspešno mogla odvijati i emisija kognitivnog radija. S-metod je metoda koja bi mogla biti dodatno istražena i testirana, radi optimalnog izbora parametra L u cilju dostizanja male verovatnoće propuštene detekcije i male verovatnoće lažnog alarma kod nepovoljnog odnosa signal/šum, čime bi se postigla visoka verovatnoća ispravne detekcije kao kod pseudo Vigner-Vila i što niža računarska efikasnost kao kod spektrograma, što su i ciljevi daljeg istraživanja. Pokazano je da se adekvatnim modelovanjem može realizovati pogodno testno okruženje radi utvrđivanja performansi vremensko-frekvencijskih metoda analize signala.

U budućem radu planirana je implementacija predložene metode analize spektra na hardversku platformu softverski definisanog radija sa akcentom na optimalan izbor parametra L kod S-metode. Dalje unapređenje analize spektra je moguće tako što će se nakon detekcije vršiti analiza karakteristika detektovanog signala sa karakteristikama očekivanog signala u cilju klasifikacije.

Zahvalnica

Ovo istraživanje je deo projekta VA-TT/3/20-22, podržanog od strane Ministarstva odbrane Republike Srbije.

Literatura

[1] G. Staple, K. Werbach, “The end of spectrum scarcity [spectrum allocation and utilization],” *IEEE Spectrum*, vol. *41*, no. *3*, pp. *48-52*, 2004.

[2] I. F. Akyildiz, W. Y. Lee, M. C. Vuran, S. Mohanty, "A survey on spectrum management in cognitive radio networks," *IEEE Communications Magazine*, vol. *46*, no. *4*, pp. *40-48*, 2008.

[3] J. Mitola and G. Q. Jr. Maquire, "Cognitive Radio: making software radios more personal," *IEEE Personal Communications*, vol. *6*, no. *4*, pp. *13-18*, 1999.

[4] FCC-03-322, "Facilitating opportunities for flexible, efficient, and reliable spectrum use employing cognitive radio technologies," ET Docket, No. 03-108, December, 2003.

[5] M. Jaiswal, A. K. Sharma, V. Singh, "A survey on spectrum sensing techniques for cognitive radio," *Conference on Advances in Communication and Conrol Systems 2013*, pp. *647-660*. IEEE. 2013.

[6] M. Subhedar, G. Birajdar, "Spectrum sensing technique in cognitive radio networks: A survey," *International Journal of Next-Generation Networks*, vol. *3*, no. *2*, pp. *37-51*, June 2011.

[7] T. Yücek, H. Arslan, "A survey of spectrum sensing algorithms for cognitive radio applications," *IEEE Communications Surveys & Tutorials*, vol. *11*, no. *1*, pp. *116-130*, 2009.

[8] B. Boashash, *Time-frequency signal analysis and processing*, Elseiver LTD, 2016.

[9] W. Guibene, A. Hayar, "Joint time-frequency spectrum sensing for cognitive radio," In *International Symposium on Applied Sciences in Biomedical and Communication Technologies (ISABEL 2010)*, pp. *1-4*. IEEE. 2010.

[10] S. Monfared, A. Taherpour, T. Khattab, "Time-frequency compressed spectrum sensing in cognitive radios," In *Global Communications Conference GLOBECOM 2013*, pp. *1088-1094*. IEEE. 2013.

[11] F. Javed, A. Mahmood, "The use of time frequency analysis for spectrum sensing in cognitive radios," In *4-th International Conference on Signal Processing and Communication Systems*, pp. *1-7*. IEEE. 2010.

[12] S. M. Hiremath, S. K. Patra, A. K. Mishra, "Hard-combined cooperative spectrum sensing using time-frequency method," *In 5th International Conference on Wireless Communications, Vehicular Technology, Information Theory and Aerospace & Electronic Systems*, Hyderabad, India, 13-16. December 2015.

[13] D. Torrieri, *Principles of spread-spectrum communication systems*, Springer 2015.

[14] J. Bajčetić, D. Mikluc, "Novel method in robust radio communication emission classification," *Proceedings of the 8th Small Systems Simulation Symposium 2020*, pp. *111-116*. Niš, Serbia, February 12-14, 2020.

[15] Lj. Stanković, M. Daković, T. Thayaparan, *Time-frequency signal analysis – with applications*, Artech House, 2013.

[16] D. Bujaković, M. Andrić, B. Bondžulić, S. Mitrović, S. Simić, "Time-frequency distribution analyses of ku-band radar Doppler echo signals," *Frequenz*, vol. *69*, no. *3-4*, pp. *119-128*, 2015.

[17] T. Thayaparan, Lj. Stanković, I. Đurović, "Micro-Doppler-based target detection and feature extraction in indoor and outdoor environments," *Journal of the Franklin Institute*, vol. *345*, no. *6*, pp. *700-722*, 2008.

[18] Lj. Stanković, "A measure of some time-frequency distributions concentration," *Signal Processing*, vol. *81*, no. *3*, pp. *621-631*, 2001.

ABSTRACT

The paper analyzes the application of three time-frequency signal analysis methods for spectrum sensing in cognitive radio. The analysis was performed based on simulated and real signals for additive white Gaussian noise of different signal-to-noise ratios. The performance of the methods is analyzed through changes in the signal to noise ratio and the detection threshold, determining the probability of false alarm, the probability of missed detection and the probability of correct detection. It is shown that the methods of time-frequency signal analysis can be efficiently used for spectrum sensing with appropriate parameter optimization.

Spectrum Sensing in Cognitive Radio Using Time-Frequency Signal Analysis Tools

Nenad Stojanović, Milenko Andrić, Dimitrije Bujaković, Boban Bondžulić, Vladimir Ristić

 ISBN 978-86-7466-930-3